

# DNA-origami scaffold for NPC mimics

Nanobiology bachelor thesis

**Ranmadusha Hengst**

4543572

Supervisor:

MSc. Alessio Fragasso

Committee members:

Dr. A. Jakobi

Prof.dr. C. Dekker

Bionanoscience department

TU Delft

July 2019



# Contents

<b>1</b>	<b>Abstract</b>	<b>3</b>
<b>2</b>	<b>Introduction</b>	<b>4</b>
2.1	The Nuclear Pore Complex . . . . .	4
2.2	FG-Nups . . . . .	6
2.3	Selective transportation through the NPC . . . . .	8
2.4	Models of transport . . . . .	9
2.5	Biomimetic approaches based on nanopores . . . . .	12
2.6	Current project . . . . .	14
<b>3</b>	<b>Materials and Methods</b>	<b>15</b>
3.1	Materials . . . . .	15
3.2	Building the biomimetic DNA-origami . . . . .	19
3.3	Insertion of DNA-origami into a lipid bilayer . . . . .	24
<b>4</b>	<b>Results and discussion</b>	<b>29</b>
4.1	Optimising NSP1-oligo coupling . . . . .	30
4.2	TEM imaging . . . . .	32
4.3	AFM analysis . . . . .	37
4.4	Insertion into a lipid membrane . . . . .	41
<b>5</b>	<b>Conclusions</b>	<b>44</b>
<b>6</b>	<b>Acknowledgements</b>	<b>47</b>
<b>7</b>	<b>Supplements</b>	<b>55</b>
7.1	FG-Nup Sequences . . . . .	55
7.2	TEM . . . . .	57

7.3	AFM . . . . .	59
7.4	Gels . . . . .	61
7.5	protocols . . . . .	62

# 1

## Abstract

In eukaryotic cells, the segregation of nuclear information from the cytosol is carried out by the Nuclear Envelope, a double lipid membrane which protects the genes from cytoplasmic mutagens. To establish a connection between the cytoplasm and nucleoplasm, tiny pores named Nuclear Pore Complexes (NPCs) span through such membrane. The biological function of the NPC consists in regulating the bidirectional transportation of small molecules, like ions and transcriptional proteins, between the two compartments by imparting a selective barrier. FG-Nups are key proteins in this process, as they line the inner channel of the NPC and are responsible for the selective behaviour. Despite many models have attempted to explain the mechanism behind selectivity and substantially agree on the importance of FG-Nups in the context of nuclear transport, the exact details about how FG-Nups arrange within the NPC lumen and interact with translocating cargoes are still debated. In the current project, we illustrate an in-vitro approach to study the behaviour of purified FG-Nups, that takes advantage of DNA-origami nanotechnology. We show that it is possible to recreate a minimalistic version of the NPC by using an octagonally shaped DNA-origami as a scaffold while keeping low concentrations of magnesium in solution ( $< 1$  mM). The NPC mimic was built by coupling FG-Nups to specified locations along the inner wall of the origami. We characterized the DNA-origami structure, under different buffer conditions, before and after functionalization, by means of negative staining transmission electron microscopy and liquid atomic force microscopy. A volumetric comparison between the bare and FG Nup-coated DNA-origami provide quantitative confirmation of the success of the protein administration. We show that the incubation of a 10 times excess of proteins per binding site on the DNA-origami successfully couples the complexes together. Finally, we present our preliminary attempts at inserting a cholesterol-modified version of the DNA-origami molecule into both large and small vesicles, as well as planar lipid bilayers.

# 2

## Introduction

A biological cell is often acknowledged as the smallest unit of life. Cells are responsible for sustaining many essential processes, such as metabolism, ion transportation and protein synthesis. Many are cells also tasked with the critical duty of storing genetic information and protecting it from environmental tempering. Eukaryotic cells achieve this by compartmentalizing genes within the double-membraned envelope of the nucleus called the *Nuclear Envelope* (NE). The continuous topology of the NE is occasionally disrupted by pores, of an inner 30 nm to 50 nm diameter<sup>1,2</sup>, that control the bidirectional movement of molecules between the cytoplasm and nucleoplasm. These pores are a consequence of large cylindrical transmembranal structures, called nuclear pore complexes. Their importance to the cell is incomparable as they interface nuclear genetic information and cytoplasmic protein synthesis.

### 2.1 The Nuclear Pore Complex

The Nuclear Pore Complex (NPC) is a large and highly conserved proteinaceous machine of ~52 MDa and ~120 MDa in yeast and vertebrates, respectively, that connects the segregated cytosol and nucleus<sup>3-9</sup>. The NPC governs the selective nucleocytoplasmic export and import of small molecules, like RNA and transcriptional proteins, across the NE. A schematic overview of the NPC is presented in Figure 2.1

Approximately 30 different structural and core proteins, called nucleoporins (Nups), form the cylindrical core scaffold<sup>3,4,6,8,10-13</sup>. They are present in multiples of eight, effectively yielding a population of more than 450 Nups per NPC<sup>4,9,12-14</sup>. Nups can be classified into three architectural categories<sup>4,6,8,12</sup> that are also observed in Figure 2.1 in different colors:

1. *Structural scaffold Nups* have alpha-solenoid and beta-propellers which establish the hourglass central channel (form the scaffold layer, in blue).

2. *Membrane-spanning Nups* have cadherin folds and transmembrane helices that anchor the NPC to the NE (form the membrane layer, in purple).
3. *Intrinsically disordered channel Nups* have coiled coils, RNA recognition sites and phenylalanine-glycine repeats, and are responsible for the selectivity of nucleocytoplasmic transportation (form the FG Nups layer, in white).

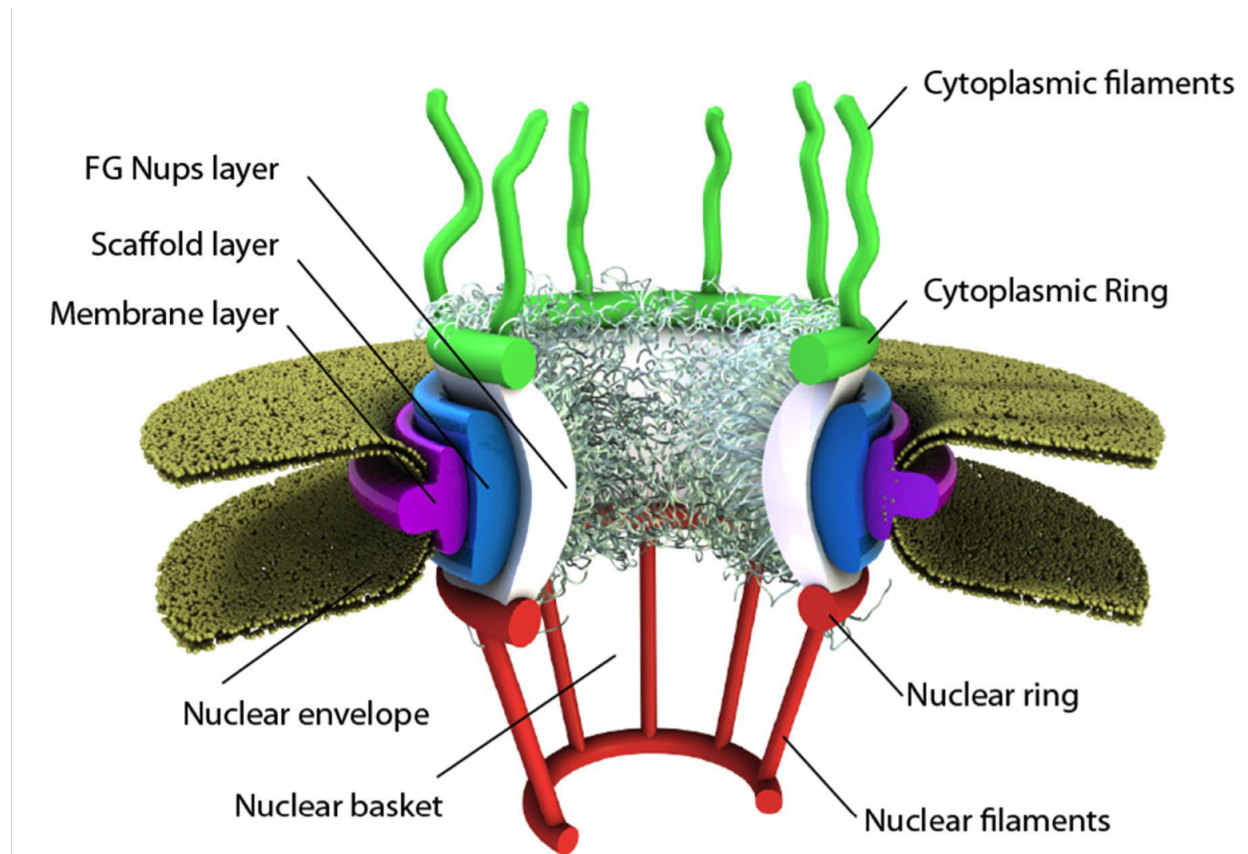


Figure 2.1: A schematic overview of the NPC. The scaffold layer (blue) spans around the pore and is connected to the NE by a membrane layer (purple). Its inner surface is coated by a layer of intrinsically disordered Nups (white). On the cytoplasmic side, the cytoplasmic ring (green) extends into eight cytoplasmic filaments, while on the nucleoplasmic side the nuclear rings (red) extend into nuclear filaments that form a nuclear basket. Adapted from Azimi, et al. 2013<sup>15</sup>

The Nups appear to segregate and assemble into organised structures, referred to as ‘*spokes*’. The NPC displays a radial eightfold-symmetry<sup>4,12</sup>. This originates from eight spokes that radially span the central channel. Each spoke can be sub-divided into nuclear and cytoplasmic filaments, which connect to form the coaxial nuclear and cytoplasmic rings of the central scaffold<sup>4,9,12,13</sup>. This scaffold plays a vital role in the maintenance of stability and co-planarity of the NE’s inner and outer membranes<sup>12</sup>.

Figure 2.2 presents a basic cross-sectional overview of the individual components of the NPC from the yeast, *S. cerevisiae*. Natively, the transmembranal complex weights approximately 86.9MDa and extends to a diameter of  $\sim 98\text{ nm}$ <sup>9,12</sup>. This translates to a typical pore diameter of  $\sim 38\text{ nm}$ <sup>6,12</sup>.

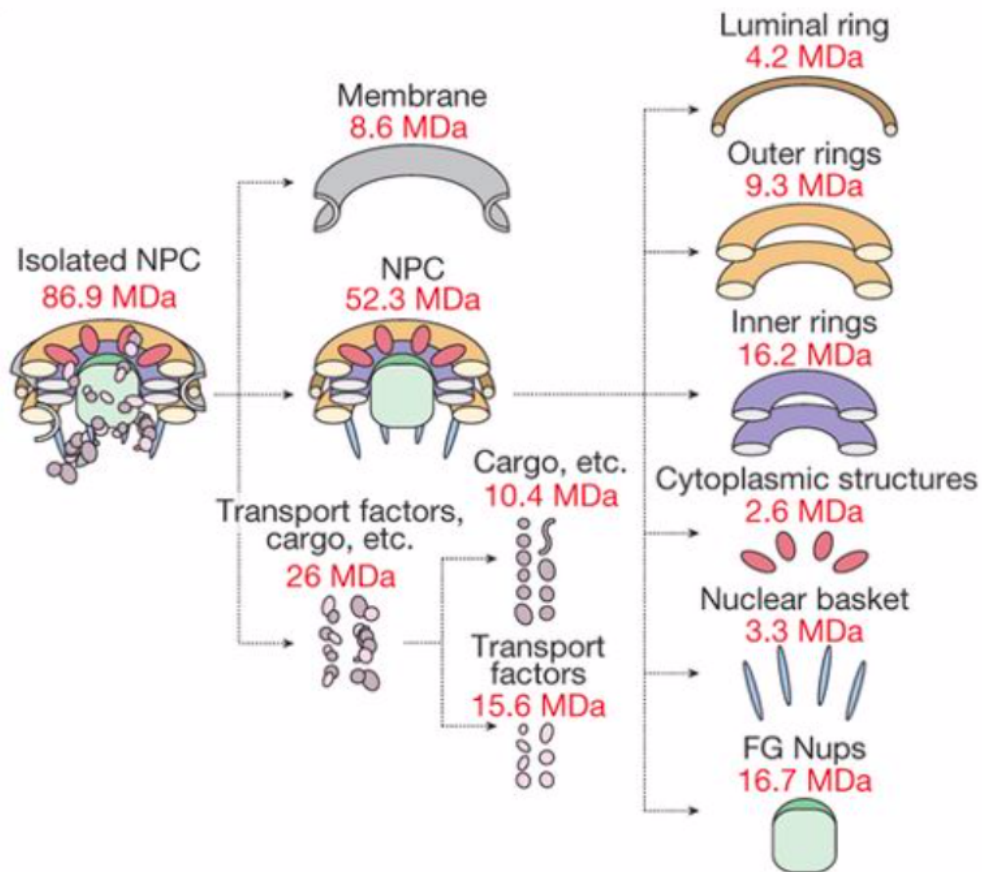


Figure 2.2: A schematic overview of yeast (*S. cerevisiae*) NPC, broken down into the individual components. A native NCP weighs at 86.9MDa out of which only 52.3MDa belongs to the NPC scaffold. Adapted from Joon Kim, et al. 2018<sup>9</sup>

## 2.2 FG-Nups

There are approximately 10-12 different intrinsically disordered proteins that line the central channel of the NPC. These proteins are more often referred to as 'Phenylalanine Glycine'- nucleoporins or FG-Nups<sup>3,4,11</sup>. As the name suggests, FG-Nups are rich in hydrophobic Phenylalanine (F) and Glycine (G) repeats and are often identified by their characteristic GLFG, FxFG, and FG motifs.

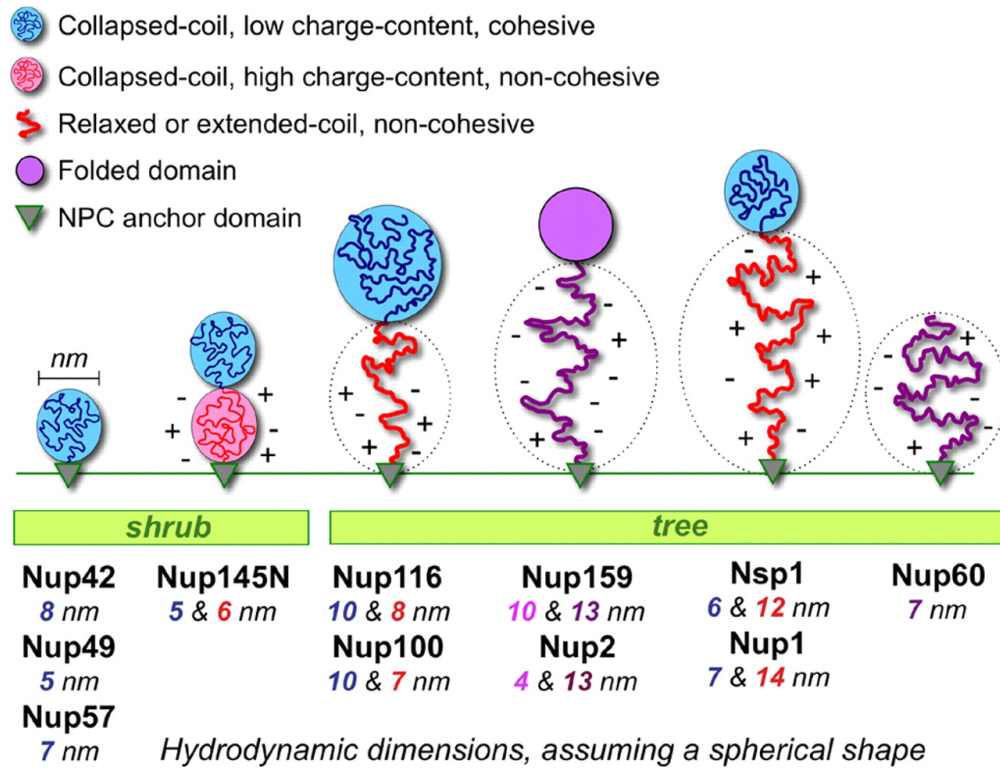


Figure 2.3: Differences between ‘Shrubs’ and ‘Trees’<sup>13</sup> Nups are categorized as shrubs if FG-Nups adopt collapsed coil configurations and are adjacent to the NPC anchor domain. FG-Nups are trees if their configuration is relaxed or has an extended coil domain separating a collapsed coil or folded globule from the NPC anchor domain. Adapted from Yamada, et al. 2010<sup>13</sup>.

In the GLFG repeat, L is the non-polar amino acid *Leucine* while in the FxFG repeat, x is a small residue such as non-polar Serine, or polar Glycine or Alanine. One FG-Nup can possess approximately ~190 of these motifs, causing an entire NPC to compromise more than 2000 FG motifs in total<sup>4,11,16</sup>. Spread from the cytoplasmic periphery to the nuclear baskets, different FG-Nups appear to localize to different positions, forming a diversely populated channel<sup>3,9,12,13</sup>. As discussed in depth in a paper by Yamada et al. 2010<sup>13</sup>, FG-Nups can form collapsed domains that coil up at different lengths from the anchor points, depending on their cohesive nature (Figure 2.3). Cohesive FG-Nups, such as Nup57, are rich in hydrophobic GLFG repeats and adopt a globular collapsed coil near the channel wall. Less-cohesive FG-Nups, like NSP1, form extended coils which can protrude and occupy the central channel of the NPC<sup>1,6,11,13,17</sup>. The interplay between different FG-Nup lengths and cohesive strengths establishes a robust selective gateway<sup>1,3,4,13</sup>.

## 2.3 Selective transportation through the NPC

Bidirectional transportation is controlled by a selective diffusion barrier that acts upon macromolecules, e.g. metabolites, RNA molecules, histones and ribosomal units<sup>1,8,11</sup>. The mesh of FG-Nups in the central channel of the NPC imposes a size-restriction on molecules larger than a weight of 20 kDa to 40 kDa<sup>1,6,8,11</sup>, while smaller particles, e.g. ions, may indiscriminately translocate across the complex at rates inversely proportional to their size<sup>18</sup>. Large macromolecules that exceed the size-limit can pass through the NPC by binding to nuclear transportation receptors (NTRs), such as Karyopherins (Kaps/importins/exportins)- the largest family of NTRs. Kaps can weigh up to ~120 kDa (Kap121) and bind to nuclear localization signals (NLS) or nuclear export signals (NES), the amino acid sequences that tag transportable macromolecules for import or export respectively<sup>1,4,6,8</sup>. In Figure 2.4, a schematic representation of the movement of Kaps through the NPC is presented. Once attached to its cargo, hydrophobic pockets on the Kap outer surface are presumed to transiently bind to the intrinsically disordered FG-Nups such that it may pass through the complex<sup>1,8</sup>. One Kap may bind several FG-Nups as the number of pockets may range from 2 to 10 per Kap<sup>8</sup>.

The directionality of transportation is driven by the concentration gradient RanGTPase (members of the Ras superfamily of proteins) that interacts with the Kaps<sup>1,3,8,20</sup>. For nuclear importin, Kap-cargo complexes travel from the cytoplasm to the nucleus, where they disassemble upon allosteric binding of the Kap to RanGTP. The importin Kap is recycled back into the cytoplasm by RanGTP, which consequently hydrolyses into RanGDP by the action of RanGAP, which causes the unbinding from the Kap. RanGTP is also involved in the assembly of the exportin complexes. The trimeric assembly, of RanGTP and the Kap-cargo complex, transports into the cytoplasm through the NPC and then dissociates upon GTP hydrolysis<sup>1,3,8,20</sup>.

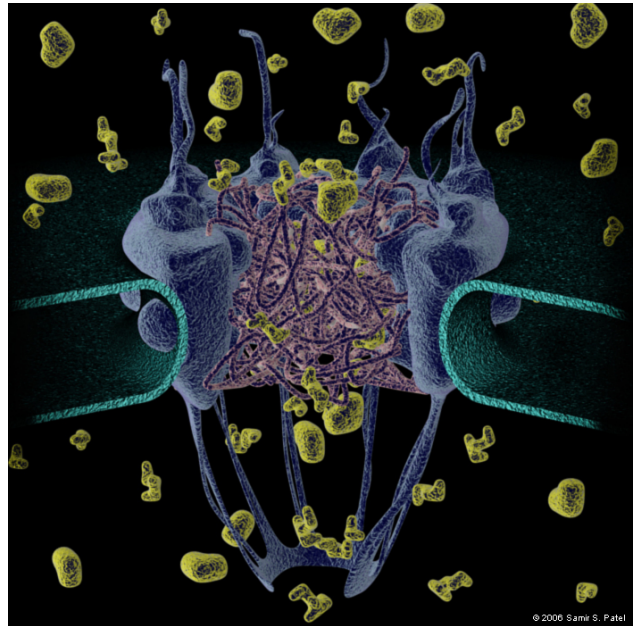


Figure 2.4: A schematic representation of Kap movement through the NPC. Taken from Samir S. Patel 2006<sup>19</sup>

## 2.4 Models of transport

Despite the effort to characterise the FG-Nups, the structure of the FG mesh barrier is still unknown<sup>1,1,4,6,6,13,21,22</sup>. Immunolabelling, TEM and AFM, have been used in an attempt to unravel the uncertain conformations. However, these techniques produce insufficiently detailed information for *in vivo* conditions<sup>1,6,8</sup>.

The biophysics of the interaction between Kaps and FG-Nup is frequently brought into question as well. The transient interaction between Kaps and FG-Nups has been proven to facilitate the selective translocation of larger cargoes<sup>1,5,7,8,11,22,23</sup>. The inquiry into the exact mechanisms behind the transmembranal movement is uncertain due to two major reasons: (1) the unresolved structure of the native FG-Nup barrier and (2) the poorly understood NTR partitioning and efficient translocation through the FG-Nup barrier. On either side of this divide lie the FG-centric and Kap-centric paradigms that attempt to explain translocation<sup>4,6,24</sup>. The two paradigms are presented in Figure 2.5. FG-centric models propose that selective translocation is regulated by the FG-barrier alone and that Kaps are not detained within the NCP channel. The Kap-centric model contradicts this paradigm by predicting the necessity of Kap occupancy within the pore.

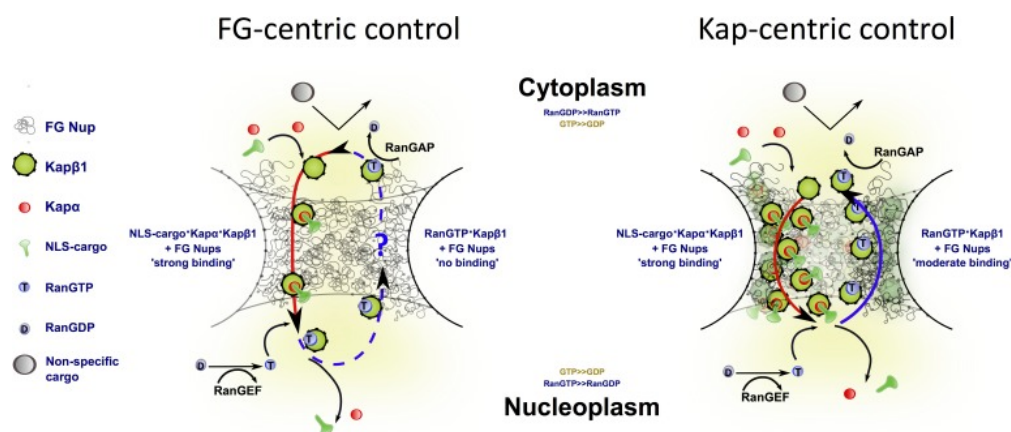


Figure 2.5: FG-centric vs Kap-centric paradigms. On the **left**, the FG-centric paradigm shows the movement of kap-cargo complexes through the FG-barrier without retention. On the **right**, the Kap-centric paradigm is driven by the occupancy of Kaps in the pore. Extracted from Kapinos, et al. 2017<sup>24</sup>

### 2.4.1 FG-centric Paradigm

This paradigm is defined by a set of guidelines. The criteria that the FG-Nups collectively work to maintain are: 1. the  $\sim 40$  kDa molecular size restriction on passive diffusion, 2. specific binding to Kaps that have sufficient binding energy, 3. conformational changes to accommodate transportation material and 4. the assistance for fast transportation<sup>6,16</sup>.

**The hydrogel model** also known as the *selective phase transitioning model*, assumes that selectivity originates from the formation of a physical meshwork of FG-Nups. Crosslinks between the proteins create the sieve-like mesh that leaves sufficient space (3 nm to 6 nm) for free diffusion of small particles but hinders translocation of larger particles<sup>1,13,21,25</sup> (Figure 2.6). Upon transient binding to the mesh, the local crosslinks are disturbed hence allowing NTRs to overcome the size restriction set by the NPC<sup>1,6,14,21,25,26</sup>. A drawback of this model is its incapability to clarify its functionality in the presence of various FG-Nup types<sup>6,21</sup>.

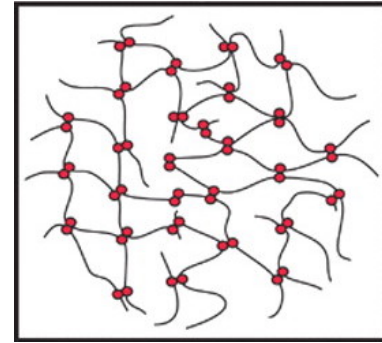


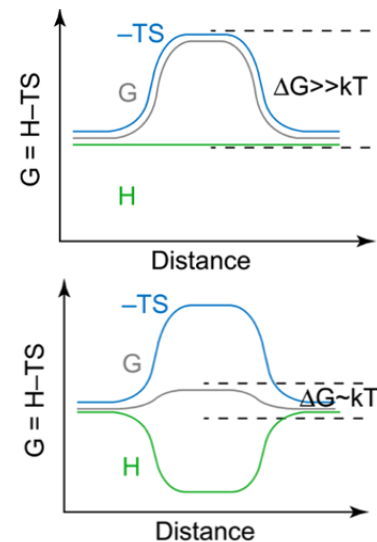
Figure 2.6: The Hydrogel model. Extracted from Frey, et al. 2006<sup>25</sup>

**The virtual gate model** predicts that FG-Nups (brushes) within the NPC impart an entropic barrier to nucleocytoplasmic transportation<sup>1,2,27</sup>.

This model could also be explained mathematically by the Gibbs free energy in formula 2.1. The Gibbs free energy ( $G$ ) available for transport is linearly dependent on the entropy ( $S$ ) of the system. A higher enthalpy ( $H$ ) decreases the net energy of the system and reduces work that must take place to overcome the entropic barrier.

$$G = H - TS \quad (2.1)$$

Figure 2.7 presents the resulting Gibbs free energy in different enthalpies. Upon encountering inert molecules, no binding takes place. This effectively means that the enthalpy is zero and therefore the entropy barrier is high. Transport factors (NTRs), unlike inert molecules, can interact with the FG-Nups. Enthalpy is introduced into the system when the NTRs bind to the FG-Nups. The increase in enthalpy counteracts the entropic barrier and therefore NTRs are able to pass through the FG-Nup barrier<sup>2,21</sup>.



TRENDS in Cell Biology

Figure 2.7: Shows the effect of enthalpy (green) on the Gibbs free energy (grey), where the entropy (blue) is constant. **Top** shows that no enthalpy (no binding) results in a high entropy barrier. **Bottom** shows that the increase in enthalpy (due to binding) lowers the barrier. Extracted from Rout, et al. 2003<sup>2</sup>

**The polymer brush model** builds upon the previous model as it also describes the influence of Brownian motion on nucleocytoplasmic transport. It defines the NPC as an entropic barrier in a way that diffusion of macromolecules becomes energetically unfavourable<sup>1,27</sup>. Entropy is introduced into the system by the FG-Nups, which are susceptible to conformational changes as dense packing generates large repulsive forces against, for example, adsorption<sup>6,29</sup>. Stochastic interaction with cargo loaded NTRs conformationally change FG-Nups such that they collapse towards the anchor points<sup>21</sup>. This generates sufficient space for the passage of the transportable complex<sup>1,27</sup>. Figure 2.8 shows an experimental example wherein the lengths of the FG-Nups shortens upon interaction with Kaps.

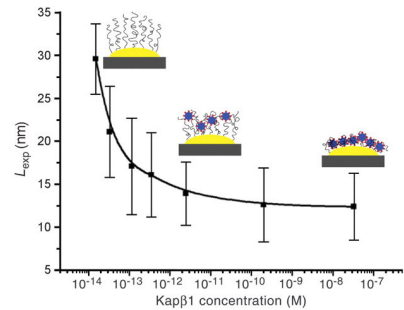


Figure 2.8: Shows the effect of Kap $\beta$ 1 on the collapse of the polymer brush. As the concentration of Kap $\beta$ 1 increases, the length range ( $L_{exp}$ ) decreases. Extracted from Lim, et al. 2007<sup>28</sup>

**The forest model** originates from the different tertiary ‘tree’- or ‘shrub’-like structures of the FG Nups that localise at peculiar lengths from the centre, suggesting functional significance in transport phenomenon<sup>6,13</sup>. This predicted behaviour can be observed in Figure 2.3, where relaxed Nups are ‘trees’.

The ‘trees’ would work as a polymer brush that regulates transportation in the central channel. The coiled domains are the ‘shrubs’ which would create a gel-like surface along the inner wall of the channel<sup>13</sup>.

A study by Yamada, et al 2010<sup>13</sup> (Figure 2.9) showed that diverse Nups with different relaxed and highly coiled domains produce an intricate pattern<sup>13</sup>. It was suggested that this arrangement could functionally influence the transportation within the NPC<sup>13,30</sup>.

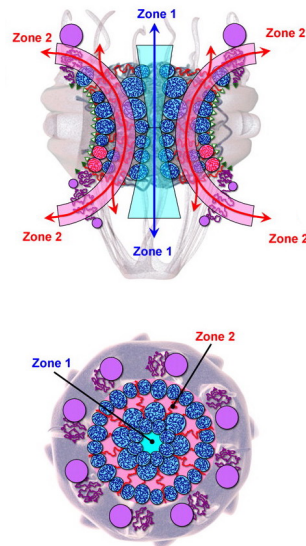


Figure 2.9: Overview of expected FG-Nup arrangement within the nuclear pore complex, as predicted by the forest model. **Top** is a cross-sectional overview of the modeled NPC. Distinct zones of transportation are highlighted in blue and red. **Bottom** is a top view of the NPC, showing different relaxation zones, through which the transportation in the *right* was observed. Extracted from Yamada, et al. 2010<sup>13</sup>

## 2.4.2 Kap-centric paradigm

The proposed FG-centric models fail to flawlessly explain the fundamental association between the FG-Nups and NTRs and the kinetics of their transport<sup>4,6,16,30</sup>. According to the FG-centric models, cargo transport is expected to occur with much slower dwell times than what is actually observed.

The Kap-centric model is able to describe the role of Kaps in controlling fast nucleocytoplasmic transportation in crowded conditions, without leading to clogging<sup>16</sup> (see Figure 2.10). The model assumes that an increased Kap concentration in the NPC limits the dimensions of movement, creating a spectrum of different kinetic behaviour upon dynamic interaction with the FG-Nups. Stronger interactions result in slower movement because of the Kap retention within the pore. Weaker interactions result in less pore retention and, therefore, faster passage. Hence, it can be said that this model potentially provides kinetic and mechanistic links to the NPC that have thus been unclear<sup>16</sup>.

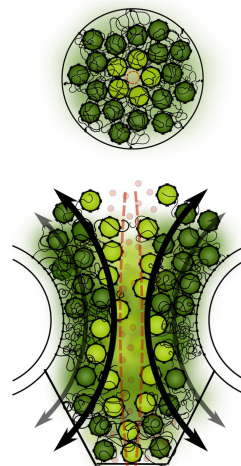


Figure 2.10: Shows the crowding of Kaps (green spheres) in transportation through the NPC. **Top** is a top overview that shows the congestions of Kaps on the top surface. **Bottom** is a cross-sectional schematic of transportation through the NPC. More dense crowding is observed along the channel periphery. Extracted from Kapino, et al. 2014<sup>31</sup>

## 2.5 Biomimetic approaches based on nanopores

The NPC is a very interesting biological machine to study, not just because of the mysterious and undiscovered mechanisms that underlie the FG-Nup and Kap interaction, but also because of its specificity towards transportable molecules. Different techniques have been developed to mimic this complex and examine the transportation of small particles through the nanometer-sized pores. In this section, we will briefly touch upon two such disciplines, relevant for the ultimate goal of this project.

**Solid-state nanopores** are nanometer-sized pores in a solid chip, often a SiN, constructed by various fabrication techniques like ion beam drilling or etching<sup>11,30,32,33</sup>. They are typically used to measure translocation of molecules through nanometer-sized pores in electrolyte buffers when exposed to a potential bias. The pore conductance may be estimated by the Nernst-planck formula<sup>2.2</sup>.

$$G_{\text{pore}} = \kappa \left[ \frac{4l_{\text{pore}}}{\pi d^2} + \frac{l}{d} \right]^{-1} \quad (2.2)$$

The surface of the pore can be further functionalised with FG Nups such that it can work as a minimalistic version of the NPC. However, these exhibit poor stoichiometric control over the Nup number and position. Furthermore, it may take several attempts to successfully coat the nanopore.

**DNA-origami nanopores** are a *de novo* biomimetic model that entails a three-dimensional structure of DNA that closely adopts the shape and dimensions of an NPC<sup>7,11,17,23,34-40</sup>. DNA is folded with high chemical and molecular precision into pre-programmed porous structures<sup>35,41,42</sup>. The surfaces of such pores can be further functionalised by FG-Nup anchor points to recapitulate the biological function of the NPC<sup>7,23</sup>. Compared to solid-state nanopores, this *de novo* biomimetic scaffold may result in better stoichiometric and spatial control over the FG-Nups within the structure, as well as high three-dimensional geometric reproducibility<sup>7,23,40,43</sup>.

Previous studies by Ketterer, et al.<sup>7</sup>, and Fisher, et al. 2018<sup>23</sup> have taken advantage of this behaviour of DNA and designed a rigid scaffold that closely resembles the dimensions of a yeast NCP. In their design, they could specify the number and locations of FG-Nup anchor points, which were defined by 21-nucleotide ssDNA handles that lined the inner surface of the ring. Fisher, et al. 2018<sup>23</sup> showed that increasing the number of handles from 1 to 48 correlated with an increased FG-Nup density at the centre of the pore<sup>23</sup>. Ketterer, et al.<sup>7</sup> managed to dock the DNA-origami FG-Nup complex on a solid-state nanopore to perform electrophoretic measurements that showed lower current vs voltage readings for coated rings.

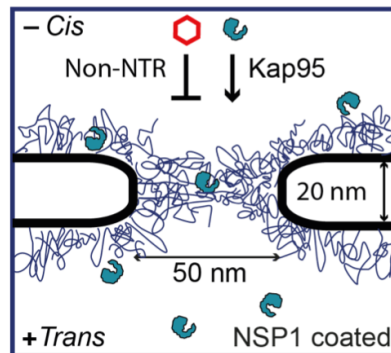


Figure 2.11: Solid-state Nanopore made of SiN membranes that are either coated in a yeast FG-Nup (Nsp1) or bare. The figure shows the expected behaviour of macromolecules through the pore in the presence of Kap and its absence. Adapted from Ananth, et al. 2018<sup>11</sup>.

## 2.6 Current project

In this project, we tested and established protocols to:

1. Build a minimalistic mimic of the NPC, combining DNA-origami and purified FG-Nups,
2. Characterise bare and FG-Nup functionalised DNA-origami with TEM and AFM, and
3. Insert bare DNA-origami into a lipid bilayer.

To meet these objectives, this project builds on the work of Ketterer, et al.<sup>7</sup> and Fisher, et al.<sup>23</sup> A *de novo* DNA-origami is the first leap towards improvement. Unlike in the previous studies<sup>7,23</sup>, we employed a structure that is both octagonally symmetric and mimics realistic NPC dimensions with an approximate inner diameter of 36 nm. The honeycombed-lattice of viral ssDNA was arranged in the shape of an octagon, which introduced the eight-fold symmetry. The inner surface of the pore was lined with 16-48 protruding oligomeric strands, distributed in a triangular lattice, which served as FG-Nup anchor points. A simplistic layout of this system with a circular DNA-origami scaffold from Ketterer, et al, lacking the eight-fold symmetry is shown in Figure 2.12

In this project, the anchor points were hybridized with FG-Nups. We subsequently imaged the obtained complexes with transmission electron microscopy (TEM) and atomic force microscopy (AFM) to analyse the coated vs uncoated octagonal DNA-origami rings. Notably, we could detect the presence of FG-Nups within the DNA-origami, thereby confirming the successful coupling.

Finally, we carried out some preliminary work into lipid membrane insertion. We found that interactions between DNA-origami and lipid surface exist, but we could not prove successful insertion. Hence, future studies will be directed towards optimizing our methods of studying lipid-DNA interaction.

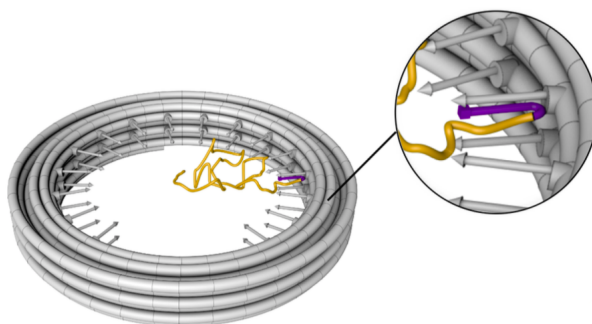


Figure 2.12: A schematic overview of the DNA-origami scaffold bound to the intrinsically disordered FG-Nup. Adapted from Ketterer, et al.<sup>7</sup>

# 3

## Materials and Methods

### 3.1 Materials

In this chapter, we discuss the material required for the construction of the DNA-origami NPC mimic. Much of this material is also required for the insertion of the lipophilic DNA pore into a lipid membrane.

#### The DNA-origami octagon

The structure of the DNA-origami octagon was designed and optimised in collaboration with the Dietz lab (Physics Department, Walter Schottky Institute, TU Munich in Germany)<sup>7</sup>. Experimental designs oblige 16 helices of modified viral *M13mp18* DNA to come together to form a honeycombed-lattice in the shape of an octagon (illustrated in Figure 3.1a)<sup>7,44</sup>. With a diameter of  $\sim 36$  nm between opposite faces and a distance of  $\sim 38.1$  nm between opposite binding sites for proteins, the robust framework of the octagonal DNA-origami exhibits 8-fold symmetry, which makes it similar to the NPC scaffold. An asymmetric feature (in blue, Figure 3.1b) was added for facilitating class averaging of EM data during data analysis (data not shown).

The surface of the octagon was furnished with a positively charged polyethylene glycol oligo-lysine co-polymer ( $K_{10}$ -PEG $_{5K}$ ) coating. The coating neutralises the negative charge of the 7560 nucleotides long single-stranded DNA and the polar glycol-group ( $OH^-$ ) in the PEG attribute prevents DNA-origami aggregation<sup>7,40,41</sup>. Additionally, the protective coating prevents nuclease degradation in low magnesium concentration ( $Mg^{+2} < 6$  mM to 18 mM)<sup>40</sup>. The resistance to unfolding at low divalent ion concentrations becomes relevant in our pursuit for near-physiological conditions ( $Mg^{+2} < 1$  mM)<sup>45</sup>.

The 4.6 MDa DNA structure rested in a buffer of 1 mM EDTA, 5 mM Tris Base, 5 mM NaCl and 5 mM  $MgCl_2$ , henceforth called 'DNA-origami buffer'. The DNA-origami buffer had a relatively

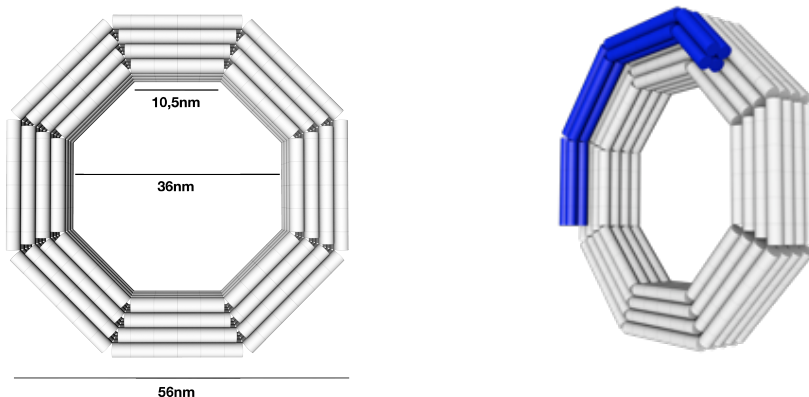
high magnesium concentration which ensured structural stability over a long period of time<sup>7</sup>. The stability of the K<sub>10</sub>-PEG<sub>5K</sub> coating has not been studied in low magnesium concentrations (<1 mM MgCl<sub>2</sub>) for more than 24 hours<sup>40</sup>.

To allow the association with FG-Nups, the octagons were armed with radially inward-pointing attachment sites. The attachment sites are also referred to as 'handles', and have the 21 nucleotide sequence:



A 38.1 nm distance between opposite handles allowed this NPC mimic approach the realistic pore diameter of 8 nm<sup>9,12</sup>. Complementary oligomeric linker molecules on the FG-Nups can hybridize to such handles, thereby allowing for a stable coupling to the origami structure.

To favour insertion into lipid membranes, the outer surface of the octagon was modified with 100 cholesterol anchors. In fact, cholesterol-modified DNA-pores have been shown to spontaneously insert into lipid membranes<sup>34-39</sup>. For the purpose of visualising lipid membrane insertion, the outer surface of the DNA-origami octagon was further functionalised with the fluorescent label, Atto647N. About 10 Atto647N molecules graced each DNA-origami octagon, their excitation and emission wavelengths corresponding to 647 nm and 661 nm, respectively. Fluorescence microscopy experiments were conducted on these molecules to observe their behaviour in vitro.



(a) Schematic of the DNA-origami scaffold (top view)

(b) Asymmetric feature (blue)

Figure 3.1: Design of the DNA-origami octagons

In this project, different variants of the DNA-origami NPC mimic were available for customised experimentation. The two major experiments of this project entailed simple coupling to FG-Nups and lipid membrane insertion. The available DNA-origami material was:

- 16 FG-Nup handles, K<sub>10</sub>-PEG<sub>5K</sub> coating and cholesterol tags (lipid membrane insertion)
- 48 FG-Nup handles and K<sub>10</sub>-PEG<sub>5K</sub> coating, no cholesterol tags (label-free imaging)
- 48 FG-Nup handles, K<sub>10</sub>-PEG<sub>5K</sub> coating, cholesterol tags and Atto647N labels (insertion in lipid membranes and fluorescence imaging)
- 48 FG-Nup handles, K<sub>10</sub>-PEG<sub>5K</sub> coating and Atto647N labels (Fluorescence-correlation spectroscopy, data not shown)
- 48 FG-Nup handles, cholesterol tags and Atto647N labels (insertion in lipid membranes and fluorescence imaging)

The octagonal DNA-origami pores were constructed at the Dietz lab by thermal cycling at a maximum temperature of approximately 65 ° C for 15 minutes. The DNA-origami spontaneously folded as the temperature was decreased by 1 ° C at intervals of an hour<sup>7,41</sup>.

### The FG-Nups

As previously discussed, native NPCs comprise a collection of thirty different nucleoporins, eleven of which make up the disordered FG-Nups that line the NPCs' central shaft<sup>1,6</sup>. In this project, we used 3 FG-Nup varieties: 1. the non-cohesive *NSP1* (65.7 kDa) with FG and FXFG repeats, 2. *NSP1-S* (62.1 kDa), the hydrophilic mutant of NSP1 (F, I, L, V are substituted by hydrophilic S) having SXSG sequence repeats, and 3. the cohesive *Nup57* 58.5 kDa, abundant in GLFG repeats<sup>7,11</sup>.

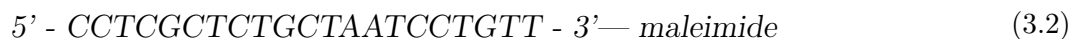
All FG-Nups were expressed in bacteria, purified and stored at -80 ° C in 5 M guanidine hydrochloride (GuHCl). GuHCl plays a characteristic role in protein stabilisation and solubility. At high (>4 Molar) concentrations, GuHCl reversibly interferes with protein folding with the consequence of a disordered structure. Upon dilution, the proteins regain their normal functionality. By storing the FG-Nups in this denaturing agent, the enzymatic activity is decreased and therefore their longevity is preserved.

A characteristic feature of NSP1-S is its inability to maintain a hydrogel conformation and bind efficiently to NTRs. Therefore, this construct may classify as a negative control.

The motivation to employ Nup57 as an additional asset to the project was to investigate the different types of spatial arrangement and behaviour as compared to NSP1.

### Oligonucleotides as a linker molecule

An interface is required to establish a connection between the nucleic acids of the DNA-origami molecule and the amino acids of the FG-Nups. The oligonucleotide-maleimide conjugate fulfils this requirement.



A 21 nucleotide sequence of single-stranded DNA ( $\sim 6.4$  kDa, complementary to the protruding attachment-sites in the DNA-origami octagon (Sequence 3.1), was conjugated to a maleimide residue (Sequence 3.2). An intermediate linker group served to reduce steric interaction<sup>46</sup>. The thiol binding group on the maleimide remained exposed for later coupling with FG-Nups. Since the oligonucleotide-maleimide conjugate, henceforth called oligo-M, becomes increasingly unstable over time if exposed to air and moisture, it was aliquoted and stored dry. The oligo-M molecules were produced and aliquoted by the biopolymer factory, *Biomers.net*.

## 3.2 Building the biomimetic DNA-origami

The first objective of this project was to reconstitute a minimalistic version of the NPC. In this section, we report the methods adopted to connect the internal surface of the octagonal DNA-origami to the FG-Nups. We further disclose the protocols followed to prepare and image the biomimetic nanopores.

### 3.2.1 Coupling of FG-Nups to oligo-M

The conjugation of FG-Nups to oligo-M to form the FG-Nup - oligo-M complex (Nup-oligo) was an essential first step in the production of a DNA-origami biomimetic nanopore. As previously mentioned, the lack of strong chemical interaction between the nucleic acids and amino acids prevents direct coupling of FG-Nups to the DNA-origami. For this reason, we used the bifunctional linker molecule, oligo-M, that has both DNA and protein binding domains. The maleimide group at the 3' of an oligo-M molecule can covalently bind to the -SH (thiol) group of the cysteine on the C-terminus of the FG-Nups. A ratio of 10:1 oligo-M to FG-Nup molecules secured optimal binding and the least loss of FG-Nups, essentially maximizing the binding efficiency. The coupling reaction was induced by a simple 1-4 hour incubation. The incubation was carried out at 25 °C and 300 rpm, in a buffer of 50 mM Tris, 0.8 M Urea, 5 mg mL<sup>-1</sup> aminocaproic acid and 2.5% 1,6-hexanediol (henceforth called buffer A). Purification and filtration of the mixture took place immediately after the incubation was complete.

The removal of unbound oligo-M and FG-Nups from the complex was performed sequentially, by the employment of AKTA ion exchange columns with buffer A and buffer B (50 mM Tris, 1 M NaCl, 0.8 M urea, 5 mg mL<sup>-1</sup> aminocaproic acid and 2.5% 1,6-hexanediol). Buffer A functioned as a running buffer when the samples were loaded onto the column, whereas the presence of buffer B would trigger the unbinding of molecules from the column in a process called 'elution'. This difference in protein binding affinity originates from the high salt (1 M NaCl) concentration in buffer B. Before and after using the AKTA purification, the columns were cleaned with buffer A and buffer B accordingly, to prevent contamination.

The movement of proteins and DNA through the columns was monitored in real-time by measuring the absorbance at 215 nm, 260 nm and 280 nm. At such wavelengths, a peak in absorbance is caused by the presence of peptide bonds and oligonucleotides, nucleic acids or aromatic amino acids (tryptophan, tyrosine, histidine and phenylalanine), respectively. The height of the peaks relates to the amount of material present, and can, therefore, provide quantitative information of the trace.

The first filtration step employed a cation exchange chromatography column (MonoS) to extract

the free oligo-M from the mixture. This strong cation exchange retains the positively charged FG-Nups within the stationary phase whilst allowing the negatively-charged molecules, the free oligo-M molecules, to flush out of the system. The retained proteins were then unloaded from the column by sharply increasing the ion concentration (elution). The electrostatic imbalance was driven by the increase of buffer B concentration in the AKTA system. The high salt molarity of buffer B (1 M) was used to screen the surface charge of the protein, therefore unbinding it from the column. All of the eluate from the MonoS column was diluted 10-20 times in buffer A to reduce the salt concentration. The diluted eluate was then loaded into an anion exchange chromatography column (MonoQ) for the removal of unbound FG-Nups. The strong anion exchange binds the negatively charged Nup-oligo in their stationary phase and allows free positively charged FG-Nups to run through.

Once all the free proteins were flushed out, the bound DNA-protein conjugates were finally eluted upon a gradual increase of buffer B. The eluate was collected in fractions of 0.3 mL. The relevant fractions were identified by analysing the absorbance at the wavelengths 215 nm (peptide bonds and oligonucleotides), 260 nm (nucleic acids) and 280 nm (aromatic proteins). Nup-oligo would correspond to a colocalized absorbance peak.

The fractions that associated with high absorption peaks were subsequently run on a sodium dodecyl sulphate-polyacrylamide gel electrophoresis (SDS-PAGE) gel for a critical assessment of the purification success. This analytical technique separates proteins (between 5 kDa and 250 kDa) according to their molecular weight under the influence of an electric field. In the process of running the gel, the tertiary structures of the proteins were destroyed and their intrinsic net charges masked. The anionic detergent, SDS, is responsible for normalising this charge to mass ratio. Firstly, SDS binds to hydrophobic amino acids on the proteins and provides a virtually uniform negatively charged coating. This effectively cancels out the effect of migration caused by charge imbalances. Secondly, upon boiling the proteins in SDS detergent, sample buffer and a reducing agent (DTT or B-ME) for 10 minutes, the inter-protein disulphide bonds are broken. The denatured protein consequently adopts a linear conformation which facilitates its movement through the mesh-like matrix of the polyacrylamide gel<sup>47,48</sup>. The gel was run for 35 minutes at 200 mV and then boiled with DI. The gel was then heated and incubated (approximately 2 hours) in *commassi blue*, before destaining it in DI. The *commassi blue* stain binds to the separated proteins, where its intensity increases with the number of proteins in the sample.

Gel-electrophoresis revealed the amount and molecular weights of the proteins in the sample. In comparison with the unbound FG-Nup, Nup-oligo showed a distinct higher band. Visual analysis of the band intensity can also provide a rough quantitative measure of the purification yield. The

brighter the band is, the greater the concentration of the fraction (given the same starting volume).

A spectrophotometer (Nanodrop, from Thermo Fisher Scientific) was employed to establish a quantification of the amount of Nup-oligo in the fractions. This device can quantify the number of proteins or DNA present in a single microliter of liquid by spectrometric analysis. With a high sensitivity (between  $2 \text{ ng } \mu\text{L}^{-1}$  and  $3700 \text{ ng } \mu\text{L}^{-1}$  for DNA) and spectral range of 220 nm to 750 nm it was ideal for our sometimes highly diluted fractions. Because of the low amount of tyrosine and absence of tryptophans in the NSP1 sequence (see Supplements, 7.1, we quantified the Nup-oligo based on absorbance corresponding to ssDNA, which generally yielded a detectable signal.

### 3.2.2 Coupling Nup-oligo to DNA-origami

When the Nup-oligos had been successfully isolated, we could finally initiate the coupling reaction of the DNA-origami to the Nup-oligo. The  $\sim 7 \text{ nm}$  handles on the inner surface of DNA-origami would hybridize at the complementary oligonucleotide sequence present on the Nup-oligo. A 10:1 ratio of Nup-oligo to DNA-origami per handle was required to ensure maximal association, essentially a surplus of 480 Nup-oligo molecules per 48-handles DNA-origami ring. To reach this ratio, we first concentrated the purified Nup-oligo by centrifuging the fractions at a maximum speed of  $13.2 \times 1000 \text{ ref}$  (relative centrifugal force) for 20 minutes through a 3 kDa cut-off filter. With a molecular mass of  $\sim 60 \text{ kDa}$ - $70 \text{ kDa}$  the Nup-oligos will not be able to pass through the filter while ions and water can leave the system. Once concentrated to mM concentrations, the Nup-oligos were added to the bare origamis and left to react overnight at  $35^\circ \text{ C}$  and 400 rpm. After the reaction was terminated, the contents were stored at  $4^\circ \text{ C}$ .

### 3.2.3 Imaging

To verify that the DNA-origami was successfully functionalised and stable, we employed two microscopy methods to visualise the samples.

#### TEM imaging

Transmission Electron Microscopy (TEM) creates high-resolution two-dimensional images of ultra-thin ( $< 100 \text{ nm}$  thick) samples by irradiating them with an electron beam of uniform current density<sup>49,50</sup>. The resolution of TEM images can reach approximately  $0.2 \text{ nm}$ . Samples (with specimens of  $\sim 1 \text{ nm}$  to  $\sim 100 \text{ nm}$  in width) are imaged on a grid (typically made of copper) that are lined with a mesh membrane<sup>49</sup>.

The grids used in this project were the CF400-Cu-UL copper grids with an ultra-thin ( $3 \text{ nm}$  to  $3 \text{ nm}$ ) carbon membrane from *Electron Microscopy Sciences*<sup>51</sup>. The 400 mesh defined a single membrane

of  $\sim 42 \mu\text{m}^2$ , which permits the analysis of hundreds of DNA-origami molecules.

Following, a negative staining protocol is presented that was developed over the course of this project.

The ultra-thin chips were pre-treated with plasma cleaning to generate a hydrophilic surface that facilitates interaction with the sample. The plasma cleaned grid surface is enriched with  $\text{OH}^-$  groups that are supposed to increase the grids' binding affinity to the uranyl stains. The grids were then treated with a single drop of sample, followed by a double washing step and a double staining step. The droplet volumes were sufficient to coat the whole grid and ranged between  $5 \mu\text{L}$  to  $10 \mu\text{L}$ . In the first step, the sample was allowed to deposit onto the grid for 30 seconds. This helped homogenize the specimen distribution on the carbon membrane. In the next two washing steps, the excess sample was removed. Furthermore, ions that could cause salt crystals aggregation with the stain were washed out. In the final staining steps, the stain was allowed to bind to the surface of the grid for 30 seconds. After removal of the stain, the grid was left to dry for 1 to 3 hours.

TEM was used to image bare and coated DNA-origami pores with 48-handles using negative staining. Negative staining requires the background to be stained, while minimally affecting the sample. We worked with three different stains during this project, all commonly associated with negative stain TEM imaging: Uranyl Acetate 2% (UA 2%), Uranyl Formate 2% (UF2%) and Uranyl Formate 1% (UF1%). Although Uranyl Acetate has a longer lifetime than Uranyl Formate, the smaller grain size and better contrast make Uranyl Formate the favourable choice. The protocols used for creating the stain are provided in the Supplementary materials.

Our first experiments with TEM probed into the stability of bare DNA-origami in different electrolyte conditions and at different points in time. By varying the magnesium levels ( $5 \text{ mM MgCl}_2$  in DNA-origami buffer to  $1 \text{ mM MgCl}_2$  in PBS, buffer A and  $10\%$  hexanediol in PBS), we attempted to test the stability exhibited by DNA-origami molecules at nearly physiological magnesium conditions<sup>45</sup>. Research by Jahnke-Dechent 2012<sup>45</sup> found  $1\%$ - $5\%$  of the  $5 \text{ mM}$  to  $20 \text{ mM}$  intercellular magnesium to be ionized in biological systems. To establish physiological conditions within our system, a magnesium ion concentration between  $0.05 \text{ mM}$  and  $1 \text{ mM}$  would be required. Further motivation to test the bare DNA-origami at low magnesium in concentration was that coupling reaction with Nup-oligo would also decrease the magnesium ion level. It was imperative to verify that the structural data of the DNA-origami molecules would not be influenced by this environmental change. Too large or small dimensions and the loss of eight-fold symmetry indicate instability due to partial or complete unfolding.

DNA gel electrophoresis can be used to discriminate between the coated and bare DNA-origami

octagons. By loading charged DNA molecules with a loading buffer of glycerol and bromodine blue into the gel, bands are observed. As with the SDS-PAGE gel, the height of the bands from the baseline indicates their size and the brightness directly correlates with the amount of DNA present in the sample. However, to run this gel the DNA-origami could not have a protective K<sub>10</sub>-PEG<sub>5K</sub> coating. Indeed, the K<sub>10</sub>-PEG<sub>5K</sub> neutralises the charge of DNA and thus hinders electrophoretic movement through the gel. As has been discussed by Ponnuswamy et al, exposure to chondroitin sulfate removes the K<sub>10</sub>-PEG<sub>5K</sub> shield<sup>40</sup>. During the reaction, the negatively charged chondroitin electrostatically sequesters the positively charged K<sub>10</sub>-PEG<sub>5K</sub> coating, subsequently allowing the DNA-origami to penetrate the matrix<sup>40</sup>. To reaffirm structural stability, the chondroitin-treated DNA-origami octagons were analysed by TEM for dimensional analysis.

### **AFM imaging**

AFM (Atomic Force Microscope) is another high-resolution imaging method, where the tapping of a cantilever measures the height of the specimen in the sample<sup>53</sup>. With a highly defined tip, AFM can reach an atomic resolution. This type of imaging is, therefore, label-free and can potentially produce high contrast output.

In this project, we employed AFM to compare the diameters and volumes of bare DNA-origami to DNA-origami functionalised with FG-Nups. A five times dilution of the DNA-origami buffer (1 mM EDTA, 5 mM Tris Base, 5 mM NaCl and 5 mM MgCl<sub>2</sub>) in PBS buffer provided near-physiological magnesium concentration<sup>45</sup>.

Prior to imaging the coated and bare DNA-origami molecules, the mica chips of the flowcell of the AFM set-up were incubated with polylysine. The negatively charged mica surface of this chip was neutralised by the positively charged polylysine layer, which facilitated DNA-origami deposition by electrostatic interaction. The DNA-origamis were imaged with instrument Bruker Multimode 8, and the cantilevers of Bruker PeakForce HIRS-F-B 1nm nominal tip radius. The sample was scanned with a 4 kHz tapping frequency and force of  $\sim 100$  pN.

### 3.3 Insertion of DNA-origami into a lipid bilayer

The final objective of this project was to study the interaction between the DNA-origami molecules and lipid bilayers. Previous studies have shown that polyanionic DNA nanostructures can accomplish this task when armed with hydrophobic molecules, such as porphyrins, tocopherol, cholesterol, or amphiphilic backbone conjugates<sup>34,36–39,54,55</sup>. Since a phospholipid bilayer is fluidic and hydrophobic by nature, it can spontaneously accommodate lipophilic molecules in a reversible process<sup>36,38,39</sup>.

Accordingly, we modified the octagonal DNA-origami rings were modified, as mentioned before in chapter 3.1, in such a way that a  $\sim 100$  cholesterol anchors extend on the exterior faces of the octagon.

We tried several approaches to achieve DNA-origami insertions.

- We tried to insert our DNA-origami into a planar lipid bilayer by subjecting it to a potential difference within an electrolyte chamber.
- We followed two strategies to insert the DNA-origami in giant unilamellar vesicles (GUVs) and image them using fluorescence microscopy.
- We created small unilamellar vesicles (SUVs) to more closely investigate the DNA-origami-lipid interactions with TEM imaging, as previous studies reported more frequent DNA insertions into highly curved surfaces<sup>34,38,55</sup>.

#### 3.3.1 Insertion on a planar lipid membrane

A lipid bilayer was built across an oil-coated  $\sim 100$   $\mu\text{m}$  aperture in a 10  $\mu\text{m}$  to 20  $\mu\text{m}$  thick Teflon film, by persistent vertical pipetting of the flow-cell mixture within a  $\sim 400$   $\mu\text{L}$  chamber. The mixture was composed by an electrolyte buffer (300mM KCl, 10mM Tris and 10mM (MgCl<sub>2</sub>)), lipids (DPHPC, from Avanti Polar Lipid, Inc.) and our modified DNA-origami. The setup was placed within a standard nanopore electrolyte box and subjected to a potential difference between charged silver electrodes.

DPHPC lipids are characteristically more stable than other traditionally used lipids, such as DOPC. The presence of methyl groups in its structure prevents disruptive fluctuations in the membrane<sup>56</sup>. Furthermore, DPHPC lipids do not have a transition temperature between 0 °C - 50 °C making it favourable for our experiment.

The lipid membrane should spontaneously incorporate the DNA-origami structures if there exists a hydrophobic affinity for the DNA-origami. With an available stock concentration of 6nM, the DNA-origami octagons had a K<sub>10</sub>-PEG<sub>5K</sub> coating, 16 internal handles and external cholesterol anchors.

The membrane was tested by subjecting it to a triangular current wave, which, in the situation that the lipid membrane was successfully spanning the Teflon hole, should be detected as a rectangular or square current response. This is an effect of the increase of capacitance due to the presence of the bilayer. Both the lipid membrane and the Teflon film insulate against current flow between the ion chambers and therefore should show no detectable conductance. Any non-zero conductance could point in principle to the formation of a channel through the lipid membrane, which can be caused by a DNA-origami insertion.

### 3.3.2 GUVs

A GUV (Giant Unilamellar Vesicle) is an aqueous droplet encapsulated by a phospholipid bilayer, whose diameter varies between  $1\ \mu\text{m}$ - $100\ \mu\text{m}$ <sup>57-60</sup>. GUVs are often used as minimalistic model systems for cells. The observed compartmentalization of fluid closely resembles cell membranes, where a complex phospholipid bilayer encapsulates the cells' contents. Their curvature and cell-like dimensions allow us to employ optical microscopes to image the GUVs. Fluorescently labelled DNA-origamis were then injected into the system to assess their interaction with the GUVs.

In our experiments, we employed two techniques to create GUVs.

**Vesicle formation by double emulsion** was derived from the traditional double emulsion method that employs glass microcapillary devices to create monodisperse double emulsions using water-in-oil-in-water phase-separation<sup>59,61</sup>. Although our approach creates spherical phospholipid bilayers from a similar phase-separation concept, we did not exploit microfluidic movement through capillaries. Rather, we maintained a cold environment in which we mixed and centrifuged the three phase-separated layers. The low environmental temperature would promote surface stabilisation of the lipid vesicles.

Figure 3.2 illustrates a brief overview of the important events of the procedure. The first identifying step is the droplet formation when mixing the top two layers. The uppermost layer, comprised of an aqueous solution mixed with the octagonal DNA-origami rings, and would constitute the internal environment of the GUV. Here, the DNA-origami rings were equipped with  $\sim 100$  cholesterol anchors, a  $\text{K}_{10}$ -PEG<sub>5K</sub> coating and 10 fluorescent labels (ATTO647N), such that it would be lipophilic, not aggregating and detectable, at the same time. The fluorescence of the DNA-origami tag could be detected at a 667 nm wavelength, which corresponds to red light.

The boundary elements of the vesicle, i.e. the lipids, are found in the middle layer. These were prepared by vacuum drying a mixture of lipids and mineral oils, followed by sonication at  $55^\circ\text{C}$ . A ubiquitous mixture of lipids,  $1\ \text{mg mL}^{-1}$  Egg(PC), mixed with  $0.05\ \text{mg mL}^{-1}$  ATTO-390 labelled DOPE-PEG, ensured a heterogeneous consistency of the layer. The heterogeneity is intuitively

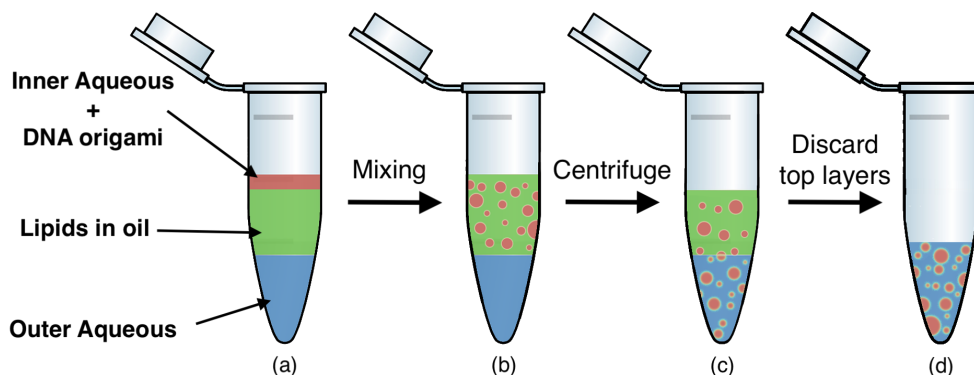


Figure 3.2: A workflow of the double emulsion process. **(a)** The top (red) layer is a mixture of inner aqueous and DNA-origami, the middle (green) layer contains the lipids suspended in mineral oil and the lowest layer (blue) contains the outer aqueous that will form the environment of the GUVs. **(b)** The top two layers are mixed and form single-layer lipid vesicles. **(c)** The sample is centrifuged to pull the single-layered vesicles into the lowest outer aqueous environment. The vesicles henceforth spanned by a double membrane. **(d)** The top layers are discarded.

thought to increase the chances of DNA-origami insertion by lowering the energy barrier due to the inhomogeneous character of the membrane. The fluorescent label on the lipids was detected at an emission wavelength of 475nm. Since this wavelength corresponds to blue light, it can be easily distinguished from the red DNA-origami. The process of mixing these two phase-separated layers establishes small droplets surrounded by a single layer of lipids (monolayer).

Next, the droplets were subjected to a centrifugal force, which pulled them down into the outer aqueous solution of the bottom layer. This was achieved by spinning the sample at 255 rcf at 4 ° C for 15 minutes in a centrifuge. Upon entering the lowest layer, the single-lipid layer of the droplet should develop into a bilayer, which constitutes the sole stable possible configuration for the droplet, hence transforming the droplet into a vesicle (or GUV). The remaining upper layers were discarded, such that only the lowest layer was imaged using either a standard fluorescence microscope or a confocal spinning disc microscope.

**Vesicle formation on a PVA substrate** exploited the swelling behaviour exhibited by lipid film coatings on dried polyvinyl alcohol (PVA) gel surfaces when exposed to an aqueous buffer<sup>62</sup>. The basic set up of this experiment is presented in Figure 3.3. As a preparatory step, simple glass coverslips were thoroughly cleaned by an ethanol-water-ethanol wash, followed by gentle drying with KimTech tissue paper. Further treatment with a plasma discharge renders the surface hydrophilic, such that it favours PVA coating. Prior to the coating, a 5% PVA solution was homogeneously warmed to 60 ° C by gentle stirring. The PVA was then gently poured onto the

coverslips, such that an approximate volume of 200  $\mu\text{L}$  would deposit on the surface. Tapping the edge of the coverslip helped establish a consistent thickness of the coating and baking (30 min) at 50 °C fixated the PVA substrate to the surface. The hardened PVA surface was then coated with a layer of Egg(PC), ATTO390 labelled DOPE-PEG and ATTO647N labelled DNA-origamis, dissolved in sucrose-enriched buffer (100 mM sucrose, 50 mM NaCl, 50 mM tris and 5 mM  $\text{mgcl}_2$ ). The PEG coating on the origami makes it slightly hydrophilic so that it does not aggregate even when functionalised with cholesterol. However, this might affect the interaction and insertion into the lipid vesicles. In order to test that, two lipophilic version, with and without  $\text{K}_{10}\text{-PEG}_{5\text{K}}$  coating), of Atto647N labelled DNA-origamis were prepared for this experiment.

Hydration of the PVA substrate, induced by adding the buffer, caused the layer to swell such that vesicles could form. These were then transferred to an environment with outer aqueous buffer (0 mM sucrose, 100 mM NaCl, 50 mM Tris and 5 mM  $\text{MgCl}_2$ ) with the same osmolarity as the inner an aqueous, but without sucrose. In this way, the sucrose-filled vesicles would sink to the bottom of the well and align on the same focal plane, thereby facilitating the imagery of vesicles. The vesicles were imaged with both standard fluorescence microscopy and confocal spinning-disc microscopy. Further addition of green fluorescent protein (GFP), with a corresponding detectable wavelength of 510 nm, helped investigate the transmembranal flow. This flow results from the opening of a channel due to the insertion of DNA-origami into the lipid membrane. A change in fluorescence due to the influx of GFP molecules in a vesicle would suggest such a movement.

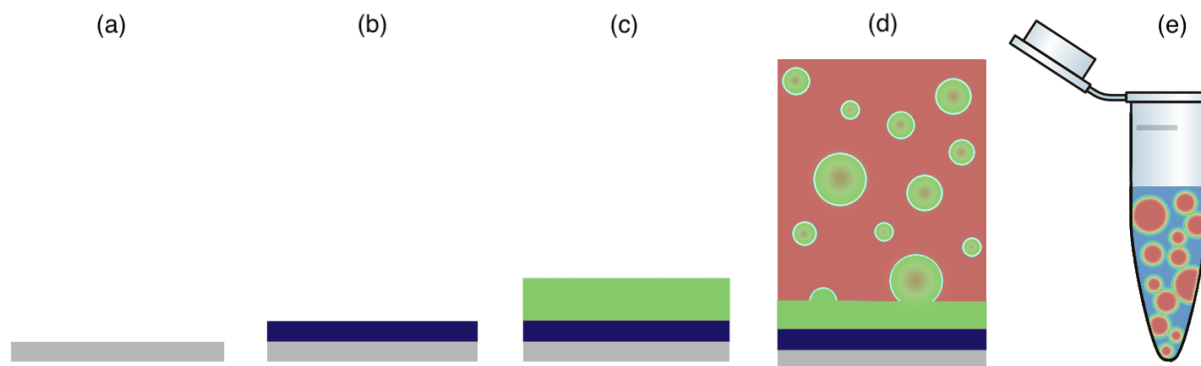


Figure 3.3: A workflow of GUV assembly on a PVA substrate. The layers added sequentially are the coverslip (grey), the PVA substrate (dark blue), the lipids (green), inner aqueous (red) and outer aqueous (light blue). **(a)** The cover-slip is plasma cleaned. **(b)** A PVA layer is deposited on the cover-slip and baked to harden. **(c)** A mixture of lipids is laid over the dried PVA substrate. **(d)** An aqueous buffer is deposited over the lipids which induces immediate spontaneous swelling of the membrane. **(e)** The vesicles in the aqueous are consequently transferred to an outer aqueous to establish the double lipid membrane.

### 3.3.3 SUVs

SUVs (Small Unilamellar Vesicle) are, in laymen terms, a smaller version of GUVs. Traditionally their diameter ranges between 15nm and 30nm<sup>63,64</sup>. Previous studies have proven that the high curvature of SUVs interacts more successfully with DNA structures<sup>34,38,55</sup>. Research by Krishnan et al.<sup>34</sup> compared the interactions between GUVs and SUVs to DNA-origami pores of a 4 nm inner diameter, and found that spontaneous insertions only took place in SUVs.

In this project, we used SUVs to verify if interactions were indeed possible between our K<sub>10</sub>-PEG<sub>5K</sub> coated DNA-origami octagons with 48-handles and the heterogeneous lipid, Egg(PC). We created two types of SUVs: neutral and negatively charged. The neutral lipids consisted of only Egg(PC) whereas the charged lipids additionally contained 10% DOPG, which adds one negative charge for each DOPG lipid molecule. The lipids were obtained from Avanti Polar Lipid, Inc.

The SUVs were formed in three kinds of environments: without DNA-origami, with DNA-origami and with lipophilic DNA-origami. The SUVs were created by means of a long dialysis process. (i) We first mixed SUVs and n-octyl-Beta-D-glucopyranoside (OG) detergent (above the 0.6% critical micelle concentration). This combination disrupts the constitution and prevents the formation of SUVs. (ii) We dissolved a 100  $\mu$ M concentration of DNA-origami octagons in a 1.5% OG in dialysis buffer (5 mM Tris pH 7.4, 5 mM NaCl and 1 mM MgCl<sub>2</sub>). (iii) The disrupted SUVs and the DNA-origami solutions were combined in a small filter cassette and to this, lipids were added at a 1 mg mL<sup>-1</sup> to 5 mg mL<sup>-1</sup> in dialysis buffer. The DNA-origami was supposed to interact with the free lipids in solution, prior to the formation of the SUV. (iv) The filter was placed in a 2 liter chamber with dialysis buffer and 0.5 g of Bio-Beads (supplied by Biomers.net) for dialysis of 3-4 days. Gentle stirring of the environment aided in OG detergent removal and hence facilitated SUV reformation once the OG detergent concentration reached below the critical micelle concentration. (v) Next, the samples were centrifuged to concentrate the diluted SUVs and incubated with a 'spatula-tips' worth of Bio-beads overnight at 4 °C to remove the last remaining detergent. At higher temperatures, the Bio-beads extract the detergent faster and therefore changes the kinetics of formation of vesicles. It is important that the environmental temperature, therefore, stays constant. (vi) Finally, the beads were removed and the SUVs imaged with TEM (the same protocol as in chapter 3.2.1)

# 4

## Results and discussion

In this chapter, we present the major results of the experiments of this project and briefly discuss their implications. More specifically, we will discuss:

- (1) how we optimised the coupling of NSP1-oligo,
- (2) the qualitative (visual) and quantitative (dimensional) analysis of bare and coated DNA-origami TEM and AFM images, and finally
- (3) the observed interaction between DNA-origami octagons and planar lipid bilayers, GUVs and SUVs.

TEM and AFM were especially important for analysing the success of the coupling experiments. They can assess the physical dimensions and characteristics by providing both, quantitative dimensional information as well a visual output that can be qualitatively analysed. Both microscopy methods have advantages over the other.

TEM has a very fast acquisition rate as it does not rely on the movement of a cantilever over the entirety of the sample. Therefore TEM can produce higher statistics at any height above the sample, without the effect of tip convolution. Additionally, TEM is more user-friendly and relatively easy to operate. A drawback is that this technique depends on sample staining and cannot differentiate between different heights in a straightforward way.

AFM, on the other hand, depends on the movement of a cantilever and therefore has a slower acquisition rate than TEM. Moreover, the output produced is therefore influenced by the tip convolution, which can lead to artefacts within the imaged sample. On the bright side, AFM allows both label-free imaging and high contrast images. Additionally, AFM experiments may be done in liquid, thereby preserving near-physiological conditions throughout the image acquisition.

## 4.1 Optimising NSP1-oligo coupling

At the offset of the project, the protocol for the Nup-Oligo coupling reaction and purification was highly theoretical and undeveloped. In previous studies, the Nup-Oligo complex was isolated by size-exclusion chromatography. This technique separates molecules based on their size and molecular weight. However, this implies that experimentation will require a high concentration of GuHCl ( $> 5\text{M}$ ), which can denature the DNA-origami. As such, a buffer exchange must take place before coupling the Nup-Oligo to the DNA-origami.

Purification with ion-exchange columns employs regular buffers (non-denaturing buffers) that are compatible with DNA-origamis for the subsequent coupling reaction to the origami. In this section, we discuss how we optimised the coupling and purification process. This protocol was optimised using NSP1 but the consistent presence of Cysteine on the C-terminal and the unwavering positive charges in the other FG-Nups implies that the protocol is applicable for the other proteins.

We encountered several problems when initially employing the ion exchange method.

(i) **Low yield** was the first essential issue faced during the first purification experiments. Starting with a gradual increase in salt concentration during elution through the anion exchange chromatography column (MonoQ) and then the cation exchange chromatography column (MonoS), the NSP1-oligo eluate became very diluted. In the process of selecting appropriate fractions, we disregarded certain fractions that may have contained the proteins, just because they went undetected through the AKTA machine. This resulted in a loss of Nup-oligo, which negatively impacted the yield of purification. We hypothesise that there is a wide range of possible binding affinities between the protein and the MonoS column, resulting in the elution of proteins over a broad range of salt ion concentrations. Upon elution, the buffer volume that passed through the system effectively reduced the NSP1-oligo concentrations up to the point that could not be detected by SDS-PAGE ( $< 10\text{nM}$  NSP1-oligo). To tackle this, we first swapped the order of the two columns, i.e. MonoS followed by MonoQ. Indeed the unbinding of the Nup- bound oligos from the MonoQ column was observed to yield much sharper peaks compared to the proteins, which is possibly due to simpler binding between oligo and the column. Additionally, we adopted a stepwise ion concentration increase during elution, which resulted in the instant unbinding of the Nup-Oligo from the column. Because of the smaller volume passing through the column, the eluate fraction was much more concentrated and therefore clearly detectable. Figures 4.1a and 4.1b present the SDS-PAGE gel before (MonoQ first, then MonoS) and after (MonoS first, then MonoQ) we optimised the order of ion exchange columns.

(ii) **Unspecific binding of maleimide** was observed as a result of both longer incubation time. Too long incubation resulted in the unspecific binding of maleimide to other amino acids, e.g. lysine. This can be seen in Figure 4.1c, where a long incubation time resulted in the observation of multiple bands. These bands could not be removed by ion-exchange chromatography since they correlate to monomeric NSP1 molecules bound to multiple oligos. The longer NSP1 and oligo-M are left in the buffer the more undesired bands form due to unspecific binding or even protein-protein dimerisation. As such: the older the reactant, the less favourable it will behave in the coupling reaction. Figure 4.1c presents the undesired dimerisation caused by old reactant.

We optimised our protocol accordingly. An incubation time of 1 to 4 hours, where the reactants were prepared right before incubation, appeared to produce the minimum amount of dimer and unspecified poly-oligo complexes. Additionally, we modified the salt ion elution gradient in column Q such that a gradual increase of Magnesium would allow different conformation of poly oligo complexes to be present in different eluate fractions. Figure 4.1d shows that different fractions from this optimisation indeed contain different poly-oligo complexes. Therefore we can isolate the Nup-Oligo monomer without having to resort to gel cutting (see Supplementary material)

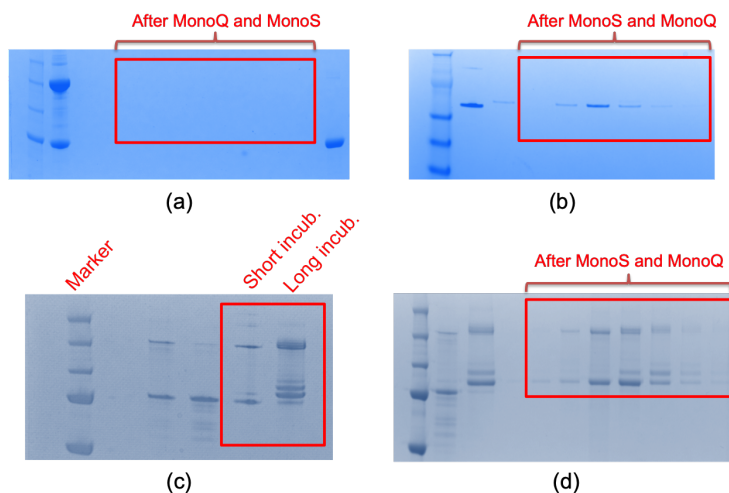


Figure 4.1: SDS-gel images of NSP1 coupled to Oligo-M. **(a)** Purification before optimisation of ion exchange does not detect any bands. **(b)** Purification after optimising the order of the columns successfully shows bands for purified NSP1-Oligo. **(c)** Longer incubation of NSP1-Oligo shows an increase in dimers. The samples were not purified but the bands suggest that Maleimide becomes less stable over time and binds unspecifically. **(d)** Shows the purified fractions from the long incubated sample in (c) can be separated by using gradient elution. Different fractions contain different bands.

## 4.2 TEM imaging

### 4.2.1 Negative staining

Just as before, no established protocol was developed for TEM imaging of DNA-origami at the start of the project. As such, we tested different stains and different grid preparation techniques to achieve desirable negative staining. In principle, negative staining does not affect the sample shape<sup>50, 52</sup> and therefore, unlike positive staining, does not add any additional bulk to the specimens. Here we will discuss how we achieved negative staining in our samples, first by comparing the effects of different stains on the DNA-origami octagons. In Figure 4.2 an overview is presented of 48-handles,  $K_{10}$ -(PEG)<sub>5k</sub> coated DNA-origami octagons discussed previously in section 3.1. Both UA and UF are positively charged stains and bind to negatively charged DNA and the plasma-activated carbon surface. However, because of their different molecular structure they bind differently to the grids and mark the DNA-origami in different ways.



The samples stained with UA 2% (Figure 4.2a) resulted in positive staining, as the samples are a darker colour than the background. Positive staining is the result of interaction between the sample and the stain, but poor interaction between the staining and the surface. Therefore, it overestimates the observed size of the DNA-origami rings and may influence the stability of the structure over time<sup>50</sup>. This undesirable effect is why we did not continue to image with UA2%.

A negative stain could be achieved with both UF2% (figure 4.2)) and UF1% (figure 4.2c) The samples appear brighter than the environment, which results from the greater interaction with the grid surface. The origamis appeared better resolved as the octagonal geometry was clearly visible. This is possibly attributed to the smaller grain size of UF compared to UA. We noted that UF2% is prone to aggregate very easily. Therefore we tried UF1% and found generally cleaner surfaces.

To further improve the cleanliness of the sample we introduced a cleaning step for UF1%. A 0.02  $\mu$ m pore filter removed a significant amount of UF aggregates. Another improvement to the protocol was the additional washing and staining steps added to the workflow. By washing the grid twice with 10  $\mu$ L drops of Milli Q diluted or removed most of the residual ions that could form salt crystals or interact with the stain in a precipitation reaction. Finally, a double staining step improved the homogeneity of the stain on the grid surface as well as the chances to obtain negative staining.

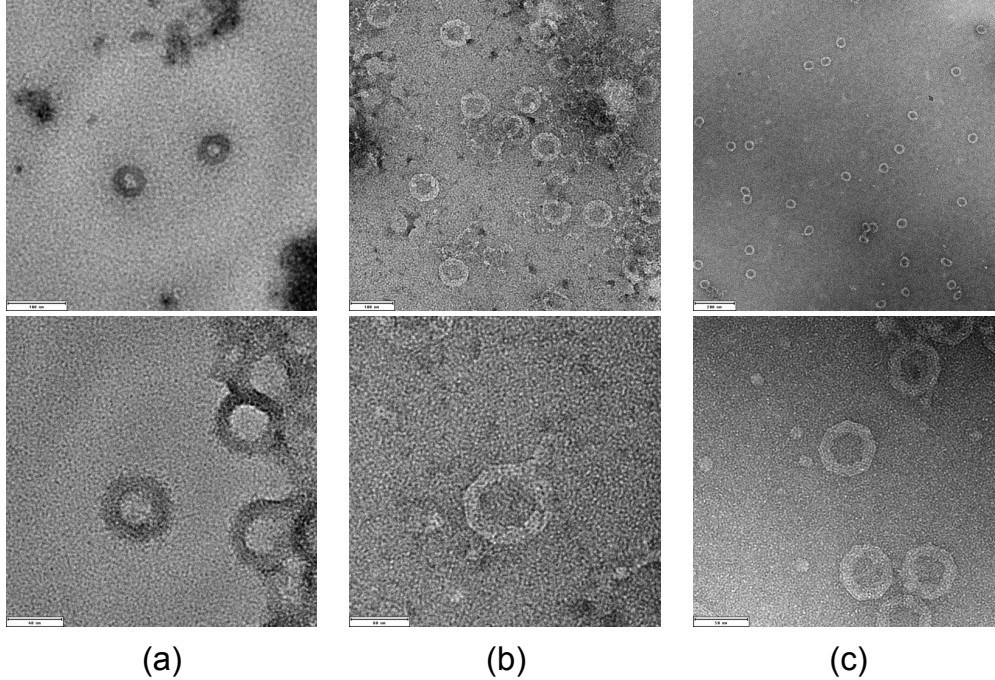


Figure 4.2: TEM images of bare DNA-origami stained by (a) UA 2%, (b) UF 2% and (c) UF 1%.

#### 4.2.2 Bare DNA-origami

Before coupling the DNA-origami pores to the FG-Nups, we tested the physical well-being of the bare DNA-origami pores in various buffers. This would allow us to study the behaviour of the DNA-origami scaffold in near-physiological conditions (e.g.  $\text{Mg}^{2+} < 5\text{mM}$ ). Upon incubation with the FG-Nups, it would be exposed a different environment from its usual 5 mM DNA-origami buffer. Incubation with the Nup-Oligo took place in buffer A which contained some denaturing agents, like the 2.5% Hexandiol and 0.8M urea, which could affect the stability of the origami.

By measuring their dimensions and visually assessing their shapes, we could estimate the stability of the DNA-origami structures. A significant deviation from the expected dimensions would indicate instability of the honeycombed lattice. Structural instability shortens the longevity of the molecules, which is undesirable for overnight incubation. In the case of unfolding, the octagonal shape of the DNA-origami would be lost, such that only an open ring or aggregate would remain in its place.

The DNA-origami octagons were imaged inside various environments with different magnesium and denaturing agent concentrations. Figure 4.3 compares the octagonal scaffold in DNA-origami buffer ( $\sim 5\text{mM MgCl}_2$ ) and 5 times diluted in PBS ( $\sim 1\text{mM MgCl}_2$ ). A first observation is that in both environmental conditions, the DNA-origami structures closely represent the expected shape

in 3.1. The octagonal shape is observed in most specimens in the images and has a consistent size. This suggests that the origami ring may indeed function as a scaffold for studying confined FG-Nups bind at near-physiological concentrations.

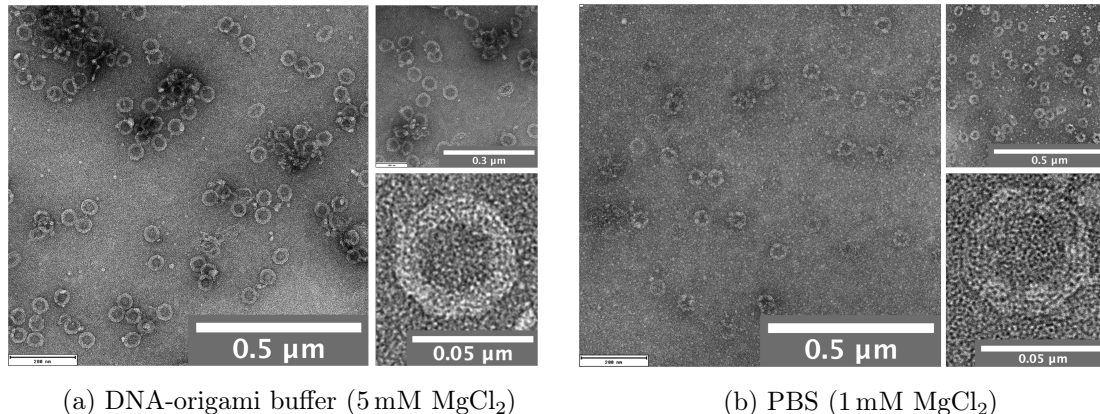


Figure 4.3: TEM images of bare DNA-origami. **(a)** Images of bare DNA-origami in 5mM MgCl<sub>2</sub> of DNA-origami buffer. **(b)** Images of bare DNA-origami diluted 5 times in PBS. It has an overall magnesium concentration of 1mM.

Upon the encouraging results, we proceeded to further study the structure of the scaffold in a 5 times dilution with Buffer A and a 5 times dilution with 10% Hexandiol concentration in PBS ( $\sim 1$  mM MgCl<sub>2</sub> in both). These buffers attempt to create unfavourable environments at low magnesium concentration. In an attempt to probe the behaviour of bare DNA-origami without the K<sub>10</sub>-(PEG)<sub>5k</sub> coating, as mentioned in section 3.3, the DNA structure was subjected to chondroitin. The structure of the scaffold was probed by dimensional analysis, to gain a quantitative estimate of the diameters of the DNA-origami pores. In a very rough measurement of the images, the diameter was calculated by measuring the cross-sectional distance between opposite internal sides of the octagon. This measurement disregarded the distinction between the vertices and edges of the structures. Geometrically speaking, the distance between opposite vertices should be larger than between opposite edges. However, for the purpose of obtaining indicative estimates, this differentiation was neglected. Figure 4.4a and 4.4b show briefly how the measurements were taken. The diameters were measured by radially spanning a linear line between the inner and outer profiles of each individual octagon. The yellow lines indicate the paths of the measured distances.

A statistical overview of the measurements in all the aforementioned conditions is presented in figure 4.4c. More details on the TEM analysis can be found in the Supplementary section. The overall average inner diameter of the octagon lies at approximately 29 nm. There is an approximate 7 nm difference between the measured inner diameter and the expected inner diameter in Figure 3.1. Similarly the measured outer diameter mismatches the expected value by 9 nm.

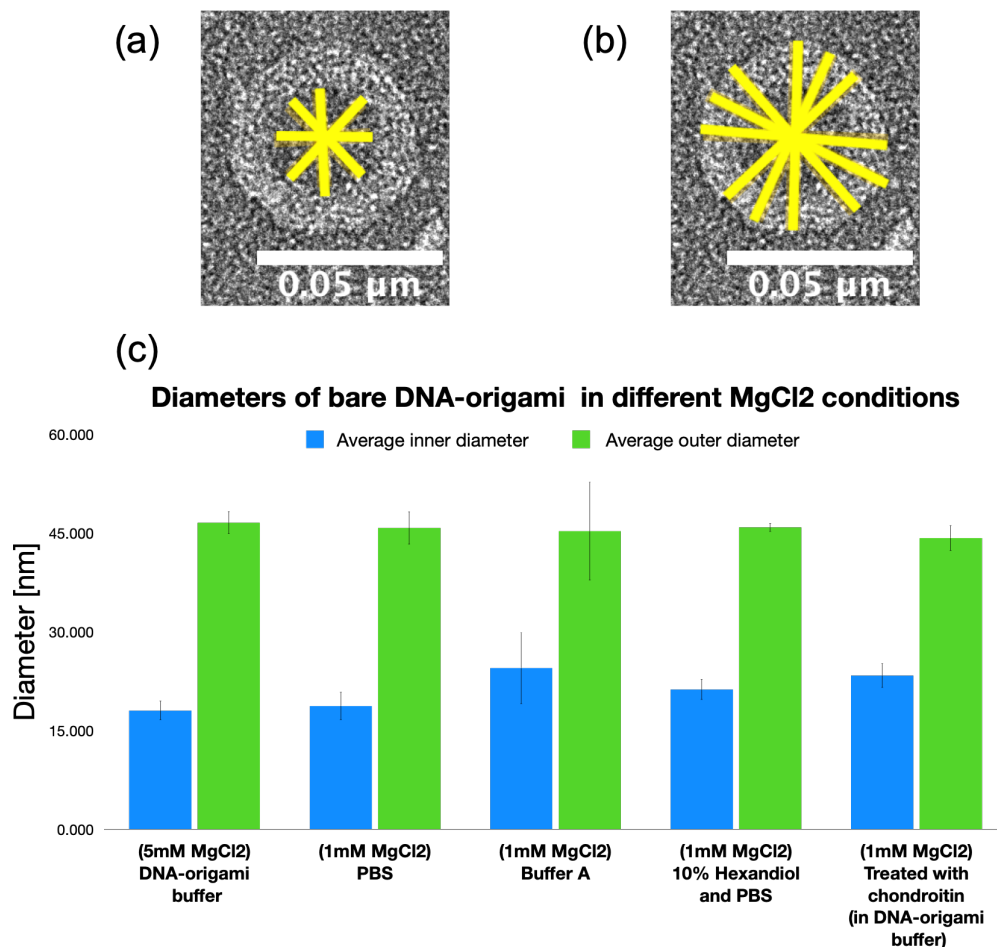


Figure 4.4: Statistical overview of measured DNA-origami. (a) Shows the the measurement of the inner diameter in 48-handles  $K_{10}$ -(PEG)<sub>5k</sub> bare octagons in DNA-origami buffer. The yellow lines represent the tracks along which the length was measured. (b) Presents a similar measurement as in (a), but for the outer diameter. c Is an overview of the average diameters and their corresponding standard deviation of NSP1 coupled DNA-origami in DNA-origami buffer, PBS, buffer A, 10% Hexandiol and PBS, and finally in DNA-origami buffer after the  $K_{10}$ -(PEG)<sub>5k</sub> removal with chondroitin treatment.

From visual confirmation, we know that the bare DNA-origami structures maintained their rigid octagonal structure. This did not change depending on the different environmental conditions introduced by the buffers.

A possible explanation for the *shrinkage* observed is the  $K_{10}$ -(PEG)<sub>5k</sub> coating, which reduces the intrinsic repulsive forces within the octagon and therefore results in a rather relaxed state of the rings.

### 4.2.3 Coated DNA

The DNA-origami-Nup complex was conjugated numerous times with NSP1 and consequently imaged with TEM. Figure 4.5 presents a few of the results of the coating process.

A first notable feature is the significantly lower concentration of DNA-origami molecules. This is agreeably an issue that has to be optimised in future experiments. The low DNA-origami amount is a consequence of a low Nup-oligo concentration after ion exchange column purification, and the fact that the proteins must be in a 480 times excess per origami scaffold

A second notable feature is an undefined mass observed within the inner rings. The irregular

but distinct shape is attributed to the presence of NSP1 bound to the inner surface of the ring.

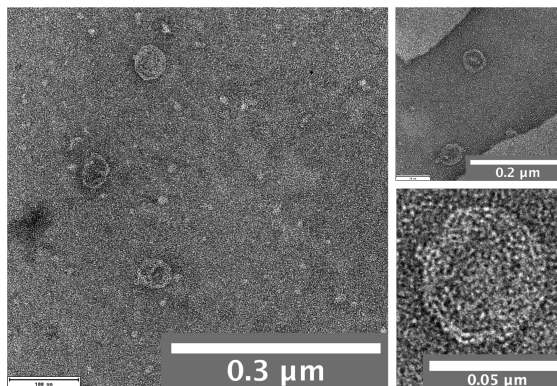


Figure 4.5: TEM images of coated DNA-origami in different scales.

Figure 4.6 presents the measurements carried out on the coated DNA-origamis, identical to those in the bare octagons. Once again a mismatch is observed between the average diameters of the measured and designed DNA-origami. The overall average inner and outer diameters of the coated DNA-origami are at  $\sim 28$  nm and  $\sim 49$  nm, respectively. These results suggest that the DNA-origami scaffold has shrunk and once again we suggest that this is the result of the  $K_{10}-(PEG)_{5k}$ .

### 4.2.4 Discussion

Over the course of time, the TEM staining and imaging technique improved as a result of the reflective process toward failed experiments. At the initial stages of imaging, there were many issues such as unwanted positive staining and other artefacts. Insufficient drying time left the grids partially wet, such that exposure to the electron beam generated stain artefacts and nanometer-sized bubbles. Stain filtration, additional washing and staining steps and increased drying time, improved the image quality significantly. Furthermore, UF1% proved to be more effective at producing negatively stained images and were less prone to aggregation compared to UF2% and UA2%.

Upon coupling the DNA-origami to the FG-Nups, the presence of proteins was revealed within the pore volume. More analysis is required to quantify the exact amount. However, this shows that origamis can be functionalised with Nups and imaged with TEM while remaining stable in near-physiological conditions.

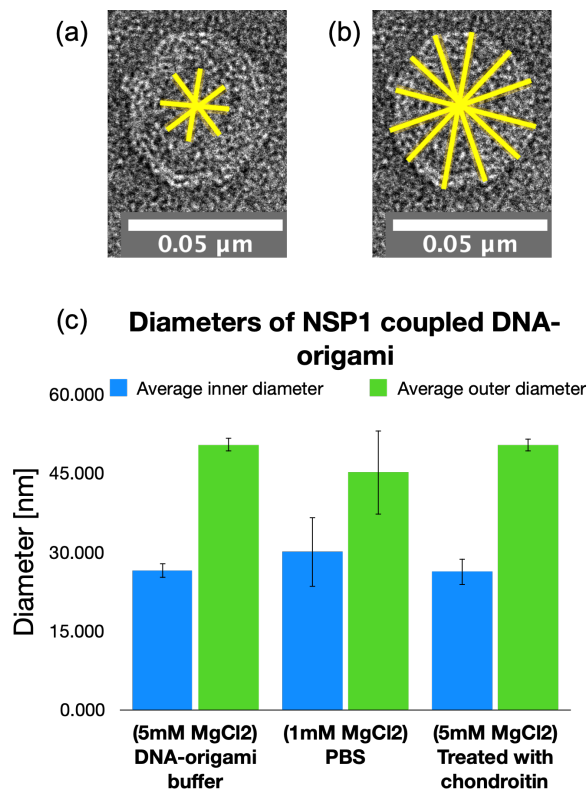


Figure 4.6: Shows the rough TEM dimensional analysis of coated DNA-origami structures in different buffers. (a) Shows the the measurement of the inner diameter in 48-handles  $K_{10}$ -(PEG)<sub>5k</sub> coated, and NSP1 coupled octagons in DNA-origami buffer. The yellow lines represent the tracks along which the length was measured. (b) Presents a similar measurement as in (a), but for the outer diameter. c Is an overview of the average diameters and their corresponding standard deviation of NSP1 coupled DNA-origami in DNA-origami buffer, PBS, and in DNA-origami buffer after the  $K_{10}$ -(PEG)<sub>5k</sub> removal with chondroitin treatment.

### 4.3 AFM analysis

In this section, we will discuss the structure of the 48-handle,  $K_{10}$ -(PEG)<sub>5k</sub> coated, DNA-origami octagon rings as measured with liquid AFM. As previously mentioned, AFM allows for stain-free imaging that produces high contrast, and can closely mimic physiological conditions because of a low magnesium ion level and neutral scaffold. By comparing the qualitative visual and quantitative dimensional differences between the bare DNA-origami rings (not bound to NSP1) and coated DNA-origami rings (bound to NSP1), we hoped to verify the presence of the proteins within the pore.

### 4.3.1 Bare DNA-origami

Atomic force microscopy was carried out to measure the volume of the origami molecules before and after protein functionalisation. In this experiment, tip convolution was not taken into consideration.

The AFM images and their data plots are presented in Figure 4.7. AFM has successfully reconstructed the bare DNA-origamis such that their shape appears octagonal and their dimensions slightly deviate from the designed parameters. From the cross-sectional analysis, an average diameter of  $\sim 30$  nm can be made out. This varies only slightly ( $\sim 6$  nm from the expected length).

The volume of the individual molecules was estimated by the *zero basis volume*. This approach calculates the volume between the grain surface and the zero  $z$  plane ( $z = 0$ ). The grain surface is defined as the top layer of the specimen and therefore confines the integral between such a plane it and the basis plane. The zero plane height can be altered such that it will set the data that falls below it to negative. Its, therefore, important that when calculating the volume of images, the basis plane is consistently set to a reasonable height. The volumetric analysis of the bare DNA-origami octagonal with this method revealed the average volume of the bare DNA-origami was  $\sim 12\,284.37\text{ nm}^3$

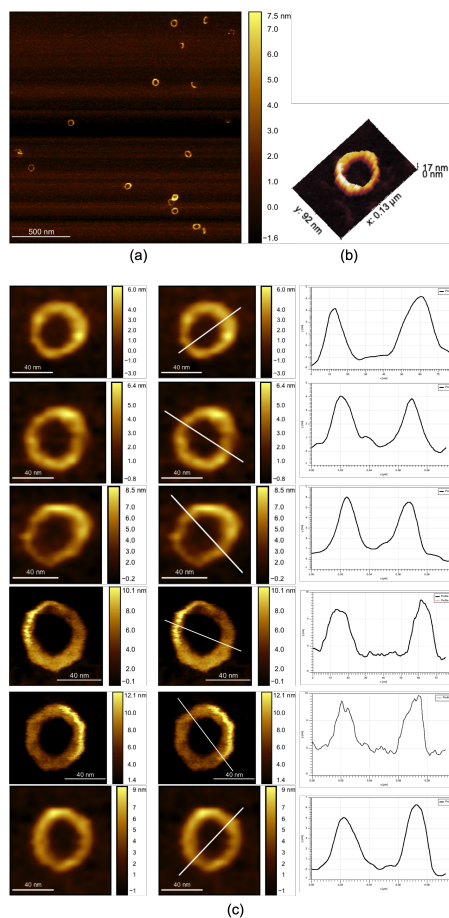


Figure 4.7: AFM images of bare DNA-origami. (a) Different bare DNA origami octagons. The scale bar corresponds to 500 nm. (b) Is a three-dimensional representation of bare DNA-origami. (c) A cross-sectional overview for bare DNA-origami octagons. The trace shows nothing to be present between the two peaks.

### 4.3.2 Coated DNA-origami

Subsequent to measuring the bare origamis, we employed AFM to analyse the DNA-origamis bound to NSP1. In this experiment, we wanted to confirm the presence of FG-Nups and possibly resolve their arrangement within the pore. This was achieved by comparing the volumes of bare and coated DNA-origamis. As mentioned previously in 3.1, NSP1 is a large and elongated molecule, with a collapsed coil on the N-terminal<sup>9,13</sup>. Importantly, NSP1 proteins are theoretically predicted<sup>9,13</sup> to interact with each other and form a dense agglomeration of collapsed-coils at the centre of the pore.

Our AFM findings are presented in Figure 4.8. As seen before, the DNA-origamis form porous structures. The sizes of the structures appear to be conserved throughout the imaged sample (Figure 4.8a). Many of the imaged structures also exhibit a notable higher density of molecules within the central pore. Structural variation is observed between the individual specimens. The peculiar external and internal commodities are detected in the majority of the coated DNA-origami rings, as was previously seen in the TEM images. Figure 4.8b shows that at the centre of the pore a high density can be detected. The corresponding histogram plots confirm that the structures are not empty. We assume that the densities are caused by NSP1.

Similar to the volumetric measurement of the bare origami structures, we employed the zero basis method to measure the average volume of the NSP1 bound DNA-origami octagons. This revealed

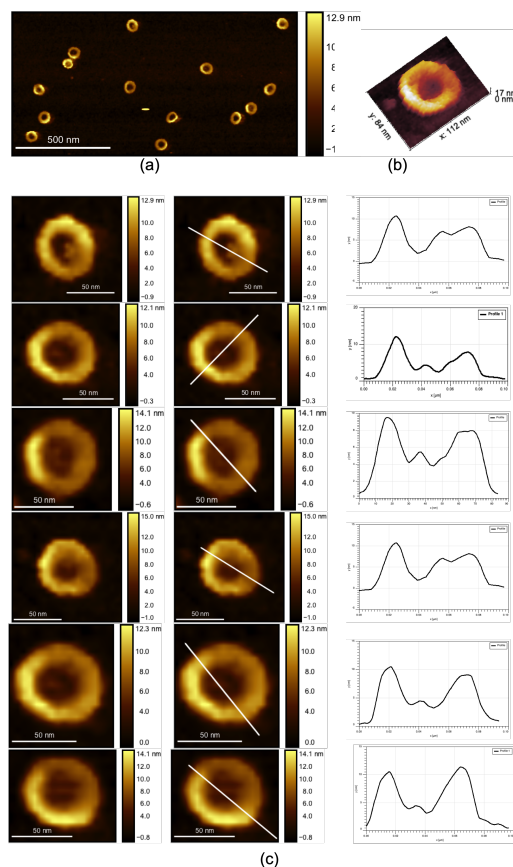


Figure 4.8: AFM images of DNA-origami coated in NSP1. AFM images of bare DNA-origami. (a) Different coated DNA origami octagons. The scale bar corresponds to 500 nm. (b) Is a three-dimensional representation of the NSP1 coupled DNA-origami. (c) A cross-sectional overview for coated DNA-origami octagons. The trace shows the density of NSP1 by heightened middle areas.

that the volumes of the coupled molecules are approximately  $\sim 25\,170.5\text{ nm}^3$ , which is almost twice as much compared to the  $\sim 12\,284.37\text{ nm}^3$  bare DNA-origamis

### 4.3.3 Discussion

Comparing the bare and coated DNA-origami molecules, a clear difference can be seen, for both their cross-sectional and volumetric measurements. In Figure 4.9, we compare these results. These results clearly show that the coated DNA-origami molecules exhibit a larger volume.

Although the bare origami structures have only a sample size of 6, there is a very large difference with the volumes of coated and bare origamis. The average volume of bare origami is  $\sim 12\,861.31\text{ nm}^3$  less than the volume of coated origami. There is no overlap between the error bars. Therefore can conclude that this data reliably confirms that the NSP1 is successfully coupled to the DNA-origami.

AFM images yielded both volumetric as well as low-noise results, with high resolution. This label-free approach has proven to successfully identify the molecular shape of the DNA-origami rings and recognise the presence of NSP1.

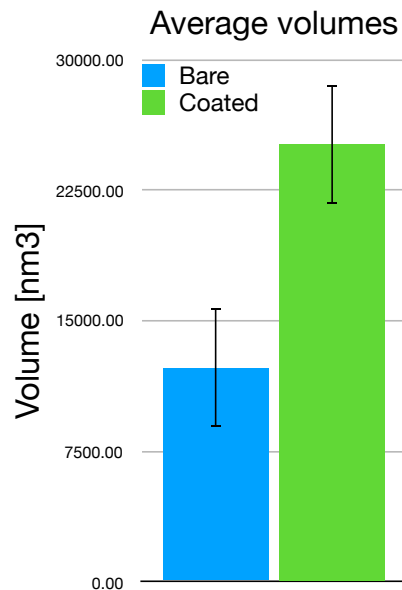


Figure 4.9: Represents volumetric data of coated and bare DNA-origami. The average bare DNA-origami volume is  $\sim 12\,284.37\text{ nm}^3$  (standard deviation of 3379) . The average coated DNA-origami volume is  $\sim 25\,145.67\text{ nm}^3$ (standard deviation of 3398)

## 4.4 Insertion into a lipid membrane

As discussed in the section 3.3, we indulged several methods to insert our uncoated 4.6MDa lipophilic DNA-origami into a phospholipid bilayer, such that it would form a pore. However, this experimentation was mainly preliminary rather than conclusive. We sought to gain more insight into the interaction between the DNA-origami and lipids.

In this section, we will briefly review the results of each experiment.

### 4.4.1 Electrostatic insertion into a planar bilayer

In this experimentation, we worked with a standard nanopore setup to insert the DNA-origami into a planar lipid layer. As explained in section 3.2.1, we build a lipid bilayer across a Teflon film. In our first experiment, a 16-handles  $K_{10}$ -(PEG) $_{5k}$  coated DNA-origami with cholesterol anchors was subjected to electrostatic forces that it would facilitate the insertion into a planar lipid bilayer. Figure 4.10 shows the shifts in the baseline during this process. We did not observe spontaneous insertions at low or zero biases and therefore increased the bias to destabilise the membrane. The corresponding stepwise behaviour of the transitions was briefly speculated to be a sign of DNA-origami insertions. However, it has been reported in studies<sup>65</sup> that this phenomenon is the result of electrostatically induced tears in the lipid bilayer, more commonly referred to as: 'electroporation'. Exposure to high electrostatic field strength reversibly destabilises membrane such that they rearrange to form aqueous pores.

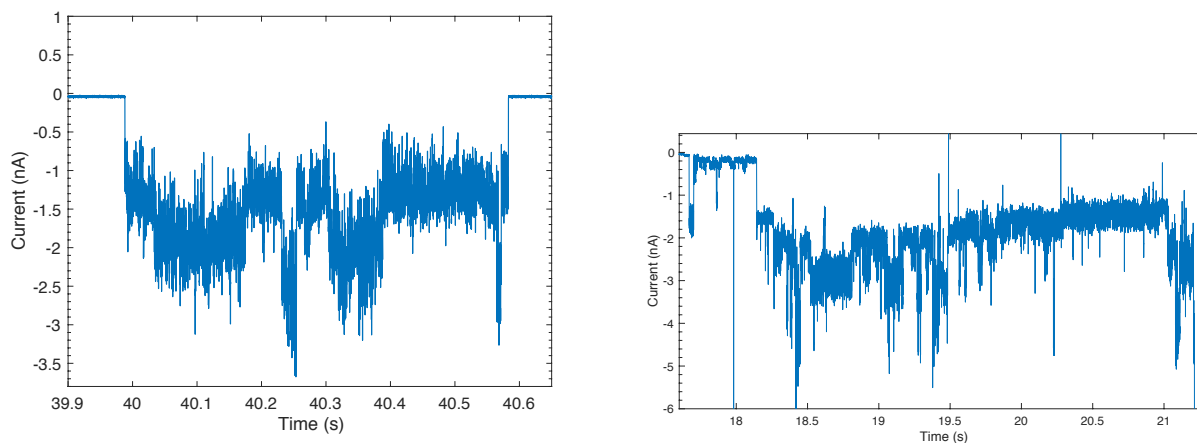


Figure 4.10: Current traces show transitions in the base current. The shifts correspond to spontaneous fragmentation in the membrane topography through which ions can carry the current

We confirmed the observed phenomenon by repeating the experiment without DNA-origami (data not shown). Indeed behaviour is similar to the transitions seen in Figure 4.10. The system

can be, however, greatly improved by reducing the chamber fluid of the flow-cell (now at  $\sim 400 \mu\text{L}$  and increasing the concentration of the DNA added. Because of the unavailability of smaller chambers, we could not carry out more experiments to test different conditions.

#### 4.4.2 GUVs

The GUVs created by both the spinning and the swelling approaches (see section 3.3) delivered a decent quality of vesicles. A distinct difference between these two methods is that in the first approach (double emulsion), the DNA-origami was present during the vesicles creating, while in the second approach (on a PVA substrate), the DNA-origami were added from the outside right before imaging the vesicles. Figure 4.11 compares the outcomes of both procedures.

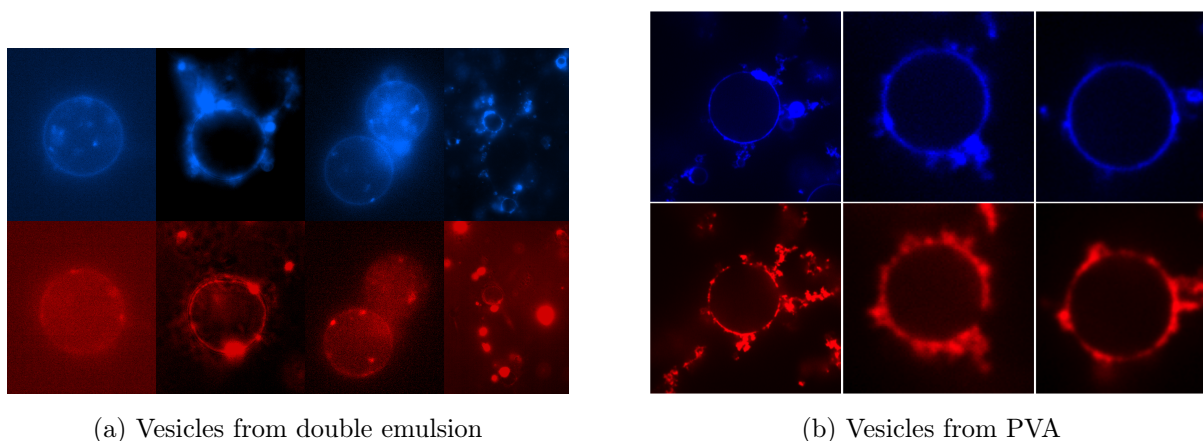


Figure 4.11: Shows vesicles of from double emulsion and PVA respectively. The lipids are shown in blue (ATTO 390) and the DNA-origamis are in red (ATTO647N). GFP not shown.

Both approaches resulted in the localisation of DNA-origami around the vesicles. It is not possible to identify single molecular insertions into the membrane. The DNA-origamis appear to aggregate at the lipid vesicle surfaces and therefore the individual molecules could not be distinctly recognised.

Vesicles created from the PVA substrate were also exposed to GFP to examine the permeability of the membrane (data not shown). However, we did not manage to measure the change in fluorescence over time because the vesicles were constantly moving out of the frame. In future experiments, we need to improve the technique to take this into consideration.

#### 4.4.3 SUVs

Next, we attempted to insert the DNA-origami molecules in SUVs such that we could recognise interactions between the lipids and DNA. In Figure 4.12, we show the TEM images of 48-handle  $\text{K}_{10}\text{-(PEG)}_{5\text{k}}$  DNA-origamis with negatively charged and neutral lipids. The DNA-origami struc-

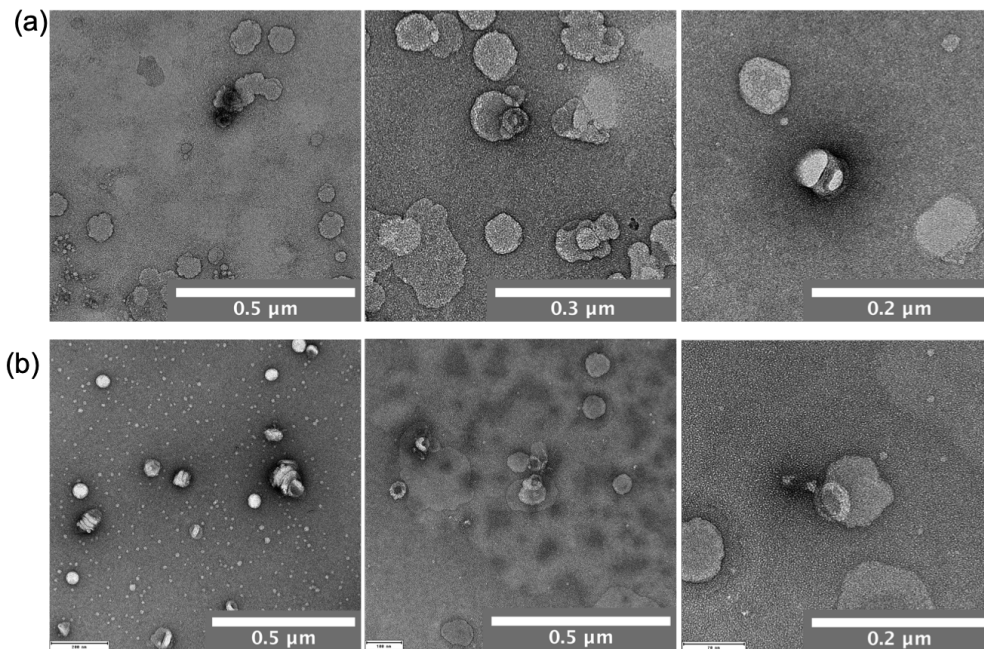


Figure 4.12: SUVs in **a** negatively charged SUVs, and **b** positively charged SUVs.

tures appear to cluster with both SUV types, and therefore we can conclude there is a certain level of interaction between lipids and lipophilic DNA-origami. There were, however, several problems observed during imaging. Because of the low amount of SUVs observed our conclusions are based on low statistics. Furthermore, the SUVs were too small. While our method should create SUVs between 20 nm to 100 nm, most observed SUVs were diametrically as large as the DNA-origami. Despite carrying out dialysis in the presence of DNA-origamis, it appeared as if the SUVs would first self-assemble before interacting with the DNA-origami octagons. We do not observe the DNA-origami octagons inside the vesicles nor do we observe insertion in the lipid membrane.

# 5

## Conclusions

Over the past 5 months, we have worked to establish a biomimetic NPC made of an octagonally-shaped DNA origami. The DNA origami was coated in a K<sub>10</sub>-PEG<sub>5K</sub> coating which aided to maintain folded stability of the origami in low magnesium concentrations. The presence of ssDNA handles along the inner surface of the octagon allowed it to hybridise with oligomeric sequences that contained a maleimide constituent. The purpose of this constituent was to form a covalent bond with the thiol group on the c-terminal of FG-Nups.

First, we investigated the structural stability of the bare DNA origamis with TEM and AFM. Indeed, both microscopy methods report the expected octagonal structure and show that this shape is conserved between the members of imaged samples. A rough dimensional analysis of TEM revealed that the inner diameter did not show much variation amongst the K<sub>10</sub>-PEG<sub>5K</sub> coated origamis. A difference in environmental conditions due to the exposure to different buffers revealed this diameter to remain almost constant. TEM, however, did show the measured diameter to be ~7 nm shorter than in the predicted model. We hypothesise that this difference originates from the positively charged K<sub>10</sub>-PEG<sub>5K</sub> coating that neutralises the negative net charge of the DNA origami. A reduction of electrostatic repulsion within the octagon appears to cause condensation of the molecule.

Next, we coupled the FG-Nups to oligo-M and conjugated this complex to the inner surface of the DNA origami. To ensure the successful coupling of Nup-Oligo, the FG-Nups were incubated in a 10 times excess of oligo-M and then optimally purified by ion-exchange chromatography columns. The DNA origami octagons were consequently incubated with a 10 times excess of Nup-oligo proteins per handle. The resultant 480 times excess FG-Nups maximized the binding efficiency to its oligomer handles. We were able to successfully couple the FG-Nup Nsp1 to the inner surface of the origami. Both AFM and TEM confirmed the observation of NSP1 within an NSP1 coated DNA origami. Interestingly, the proteins formed a globular aggregation within the inner channel of the

pore.

The volumes of the bare and coated DNA origami were measured in liquid-AFM. Within this setup, physiological conditions such as low magnesium concentrations ( $\sim 1$  mM) and a neutral binding surface were maintained. A comparison between the two revealed that coated DNA origami structures had a consistently larger volume. Although this measurement does not quantify the amount of NSP1, it does provide evidence that the coupling reaction was successful.

To establish a biomimetic nanopore and prove the selective functionality, the coated DNA origami must be docked onto a supporting membrane in order to measure its transport properties. Previous studies<sup>7,11</sup> have discovered that the docked origamis on solid-state nanopores, increase substantially the  $1/f$  noise during electrolyte experiments. For this reason, we investigated the interaction between DNA origami and lipid membranes, as the complete integration of the octagonal pore into the bilayer is expected to generate less noise. Prior experiments have shown that DNA nanostructures can insert into lipid membranes if rendered lipophilic by the addition of hydrophobic groups along its outer surface<sup>?,34,36-39,54,55</sup>. In parallel with the previously described experiments, we also ventured to recognise interactions between lipids and bare K<sub>10</sub>-PEG<sub>5K</sub> DNA origami with ( $\sim 100$ ) cholesterol anchors in 1. planar lipids bilayers (electrolyte experiments), 2. GUVs (fluorescence microscopy) and 3. SUVs (in negatively stained TEM).

These experiments did not divulge much about the inherent interactions. Planar lipids did not show spontaneous insertions of DNA origami because of its low (several pM) concentration in the 400  $\mu$ L electrolyte chamber. Our measurements were therefore hindered by the scale of the setup. GUVs revealed the aggregation of DNA origami molecules at the interface between the lipid vesicles and the environment. We did not manage to make a time-lapse of the change in GFP fluorescence within pores to observe the influx of the GFP molecules through inserted DNA origamis. Finally, experimentation on SUV could not provide further insight into the DNA-origami and lipid interaction. The yield of SUVs was too low and their small dimensions failed to integrate the large DNA origami molecules.

### **Future perspectives**

After having established evidence for the coupling of DNA origami molecules to NSP1, we look into the next opportunities. Future projects may attempt to continue the coupling of DNA origami molecules to different FG-Nups (e.g. NSP1-S and Nup57 as mentioned in section 3.1). AFM and TEM may reveal the different spatial densities within the pore. These results may, therefore, verify the forest model proposed by Yamada et al<sup>13</sup>. According to this model, we expect a globular density of Nup57 near the periphery of the pore, whereas a more extended conformation in the case of NSP1.

A next project may also probe the net amount of FG-Nups bound to the inner surface of the DNA origami octagon. By labelling oligo-M with cyanine-5 (Cy-5) it would be possible to count the number of hybridized handles in the pore. Additionally, fluorescence correlation spectroscopy optically quantifies the labelled molecules by analysis single photons that are emitted by the fluorophores. Binding affinities between labelled origamis and different cargoes could potentially show selective properties of the FG-Nup coated origamis.

More opportunities for research are presented by the ineffective measurements in the lipid and DNA-origami interaction. As previously mentioned, certain improvements to the different methods would increase the likelihood of observing desired interactions.

1. Electrolyte measurements with planar lipid bilayers could be achieved in flows-cells of a much smaller chamber. We suggest a chamber of a few tens of  $\mu\text{L}$ . Within such small volumes, the concentration of DNA is much higher and therefore there is a greater chance of successfully inserting DNA origami into a bilayer.
2. The influx of GFP in GUVs with and without origamis can be studied over a period of time by recording a time-lapse. An increase of fluorescence intensity within the vesicles indicates the presence of a pore in its membrane.

# 6

## Acknowledgements

I would like to thank a few people, without whom this project would not have been possible.

First of all, my supervisor MSc. Alessio Fragasso, who guided and supported me through all experiments. He operated the TEM, taught me how to make the buffers and run the gels, optimised the protocols and designed the experiments.

I want to thank research technicians Jaco van der Torre, Eli van der Sluis and Allard Katan. Jaco and Eli helped us run the ion-exchange chromatography purification and many of the gels. Allard imaged our DNA-origami samples with liquid-AFM and provided us with all the images used in our analysis.

I want to thank Nicola De Franceschi for helping us make the GUVs and SUVs, Sonja Schmid for helping us with building the planar lipid membranes and Paola De Magistris for providing us with the Nup57 protein.

I thank Alberto Blanch Jover for helping us create GUVs, run the ion-exchange chromatography columns and showing us how to run the SDS-PAGE gel and graduate student Wayne Yang for showing us how to run the negative stain protocol in TEM imaging.

I want to show my appreciation to Dr. A. Jakobi. He supplied the uranyl formate for our TEM experiments and helped us optimise our negative staining protocol.

I want to thank everybody at the Cees Dekker lab for being so accommodating and guiding me through this project.

Finally, I thank Cees Dekker for accepting me into this lab. It has been an unforgettable educational experience.

# Bibliography

- [1] S. Terry, L. andand Wenté. Flexible gates: Dynamic topologies and functions for fg nucleoporins in nucleocytoplasmic transport. *Eukaryotic Cell*, 8(12):1814–1827, 2009.
- [2] Michael P Rout, John D Aitchison, Marcelo O Magnasco, and Brian T Chait. Virtual gating and nuclear transport: the hole picture. *Trends in cell biology*, 13(12):622–628, 2003.
- [3] Susan R Wenté and Michael P Rout. The nuclear pore complex and nuclear transport. *Cold Spring Harbor perspectives in biology*, 2(10):a000562, 2010.
- [4] Reiner. Translocation through the nuclear pore: Kaps pave the way. *BioEssays*, 31:466–477, 2009.
- [5] Stefan W Kowalczyk, Larisa Kapinos, Timothy R Blosser, Tomás Magalhães, Pauline van Nies, Roderick Y H Lim, and Cees Dekker. Single-molecule transport across an individual biomimetic nuclear pore complex. *Nature Nanotechnology*, 6:433, jun 2011.
- [6] Daniel A. Kraut Andreas T. Matouschek|| Roderick Y. H. Lim⊥ Bin Xue Lukasz Kurgan Monika Fuxreiter, Ágnes Tóth-Petróczy and Vladimir N. Uversky. Disordered proteinaceous machines. *Chemical Reviews*, 114(13):6806–6843, 2014.
- [7] P. Ketterer, A. Ananth, D. Laman Trip, A. Mishra, E. Bertosin, and M. et al Ganji. Dna origami scaffold for studying intrinsically disordered proteins of the nuclear pore complex. *Nature Communications*, 9(1), 2018.
- [8] Tijana Jovanovic-Talisman and Anton Zilman. Protein transport by the nuclear pore complex: Simple biophysics of a complex biomachine. *Biophysical Journal*, 113(1):6–14, 2017.
- [9] Seung Joong Kim, Javier Fernandez-Martinez, Ilona Nudelman, Yi Shi, Wenzhu Zhang, Barak Raveh, Thurston Herricks, Brian D. Slaughter, Joanna A. Hogan, Paula Upla, Ilan E. Chemmama, Riccardo Pellarin, Ignacia Echeverria, Manjunatha Shivaraju, Azraa S. Chaudhury,

- Junjie Wang, Rosemary Williams, Jay R. Unruh, Charles H. Greenberg, Erica Y. Jacobs, Zhiheng Yu, M. Jason de la Cruz, Roxana Mironska, David L. Stokes, John D. Aitchison, Martin F. Jarrold, Jennifer L. Gerton, Steven J. Ludtke, Christopher W. Akey, Brian T. Chait, Andrej Sali, and Michael P. Rout. Integrative structure and functional anatomy of a nuclear pore complex. *Nature*, 555:475, Mar 2018. Article.
- [10] Daniel H. Lin, Tobias Stuwe, Sandra Schilbach, Emily J. Rundlet, Thibaud Perriches, George Mobbs, Yanbin Fan, Karsten Thierbach, Ferdinand M. Huber, Leslie N. Collins, Andrew M. Davenport, Young E. Jeon, and André Hoelz. Architecture of the symmetric core of the nuclear pore. *Science*, 352(6283), 2016.
- [11] Ananth A, Mishra A, S. Frey, A. Dwarkasing, R. Versloot, and E. et al van der Giessen. Spatial structure of disordered proteins dictates conductance and selectivity in nuclear pore complex mimics. *Elife*, 7, 2018.
- [12] Frank Alber, Svetlana Dokudovskaya, Liesbeth M. Veenhoff, Wenzhu Zhang, Julia Kipper, Damien Devos, Adisetyantari Suprpto, Orit Karni-Schmidt, Rosemary Williams, Brian T. Chait, Andrej Sali, and Michael P. Rout. The molecular architecture of the nuclear pore complex. *Nature*, 450:695, Nov 2007. Article.
- [13] Samir Patel Gabriel Goldfien Alison Calestagne-Morelli Hans Huang Ryan Reza Justin Acheson Viswanathan V. Krishnan Shawn Newsam Ajay Gopinathan Edmond Y. Lau Michael E. Colvin Vladimir N. Uversky Justin Yamada, Joshua L. Phillips and Michael F. Rexach. A bimodal distribution of two distinct categories of intrinsically disordered structures with separate functions in fg nucleoporins. *Molecular and Cellular Proteomics*, 9(10):2205–2224, 2010.
- [14] David Ando and Ajay Gopinathan. Cooperative interactions between different classes of disordered proteins play a functional role in the nuclear pore complex of baker’s yeast. *Cold Spring Harbor Perspectives in Biology*, 2(10):a000562–a000562, 2017.
- [15] Mohammad Azimi and Mohammad RK Mofrad. Higher nucleoporin-importin $\beta$  affinity at the nuclear basket increases nucleocytoplasmic import. *PloS one*, 8(11):e81741, 2013.
- [16] Binlu Huang Roderick Y H Lim and Larisa E Kapinos. How to operate a nuclear pore complex by kap-centric control. *Nucleus*, 6(5):366–372, 2015.
- [17] Severin Ehret Carolina Araya Callis Steffen Frey-Murray Stewart Changjiang You Dirk Görlich Bart W Hoogenboom Raphael Zahn1, Dino Osmanovic and Ralf P Richter. A physical model describing the interaction of nuclear transport receptors with fg nucleoporin domain assemblies. *elife*, 5, 2016.

- [18] C. Dingwall and R. Laskey. Protein import into the cell nucleus. *Annual Review Of Cell Biology*, 2(1):367–390, 1986.
- [19] Samir S. Patel, 2006. [Online; accessed July 13, 2019].
- [20] Robert H. Singer and Michael Rout. Nuclear export dynamics of rna-protein complexes. *Nature*, 475(7356):333–341, 2011.
- [21] Ali Ghavami, Liesbeth M Veenhoff, Erik van der Giessen, and Patrick R Onck. Probing the disordered domain of the nuclear pore complex through coarse-grained molecular dynamics simulations. *Biophysical journal*, 107(6):1393–1402, 2014.
- [22] Cees Dekker. Biomimetic nuclear pore complexes.
- [23] P. Fisher, Q. Shen, B. Akpınar, L. Davis, K. Chung, and D. et al Baddeley. A programmable dna origami platform for organizing intrinsically disordered nucleoporins within nanopore confinement. *ACS Nano*, 12(2):1508–1518, 2018.
- [24] Larisa E. Kapinos, Binlu Huang, Chantal Rencurel, and Roderick Y.H. Lim. Karyopherins regulate nuclear pore complex barrier and transport function. *The Journal of Cell Biology*, 216(11):3609–3624, 2017.
- [25] S. Frey, R. P. Richter, and D. Görlich. Fg-rich repeats of nuclear pore proteins form a three-dimensional meshwork with hydrogel-like properties. *Science*, 314(5800):815–817, 2006.
- [26] Dirk Görlich Katharina Ribbeck. Kinetic analysis of translocation through nuclear pore complexes. *The EMBO Journal*, 20:1320–1330, 2001.
- [27] R Peters. Translocation through the nuclear pore complex: Selectivity and speed by reduction-of-dimensionality. *Traffic*, 6(5):421–427, 2005.
- [28] Roderick YH Lim, Birthe Fahrenkrog, Joachim Köser, Kyrill Schwarz-Herion, Jie Deng, and Ueli Aebi. Nanomechanical basis of selective gating by the nuclear pore complex. *Science*, 318(5850):640–643, 2007.
- [29] Larisa E. Kapinos Yusuke Sakiyama, Adam Mazur and Roderick Y. H. Lim. Spatiotemporal dynamics of the nuclear pore complex transport barrier resolved by high-speed atomic force microscopy. *Nature Nanotechnology*, 11(8):719–723, 2016.
- [30] S. Kowalczyk, T. Blosser, and C. Dekker. Biomimetic nanopores: learning from and about nature. *Trends In Biotechnology*, 29(12):607–614, 2011.

- [31] Larisa E Kapinos, Rafael L Schoch, Raphael S Wagner, Kai D Schleicher, and Roderick YH Lim. Karyopherin-centric control of nuclear pores based on molecular occupancy and kinetic analysis of multivalent binding with fg nucleoporins. *Biophysical journal*, 106(8):1751–1762, 2014.
- [32] Cees Dekker. Solid-state nanopores. *Nature Nanotechnology*, 2(4):209–215, 2007.
- [33] P. Nuttal Oliver Otto Ulrich F. Keyser-Vincent Tabard-Cossa Joseph W.F. Robertson Gaurav Goyal Kevin J. Freedman Anmiv S. Prabhu Min Jun Kim Mariam Ayub Joshua B. Edel T. Albrecht, T. Gibb and Tim Albrecht. *Engineered Nanopores for Bioanalytical Applications*. Elsevier Inc., 2013.
- [34] Swati Krishnan, Daniela Ziegler, Vera Arnaut, Thomas G. Martin, Korbinian Kapsner, Katharina Henneberg, Andreas R. Bausch, Hendrik Dietz, and Friedrich C. Simmel. Molecular transport through large-diameter dna nanopores. *Nature Communications*, 7, Sep 2016. Article.
- [35] Yong-An Ren, Han Gao, and Xiangyuan Ouyang. Advances in dna origami nanopores: Fabrication, characterization and applications. *Chinese Journal of Chemistry*, 36(9):875–885, 2018.
- [36] Oliver Birkholz, Jonathan R. Burns, Christian P. Richter, Olympia E. Psathaki, Stefan Howorka, and Jacob Piehler. Multi-functional dna nanostructures that puncture and remodel lipid membranes into hybrid materials. *Nature Communications*, 9(1):1521, 2018.
- [37] Nicole Avakyan, Justin W. Conway, and Hanadi F. Sleiman. Long-range ordering of blunt-ended dna tiles on supported lipid bilayers. *Journal of the American Chemical Society*, 139(34):12027–12034, Aug 2017.
- [38] Aleksander Czogalla, Henri G. Franquelin, and Petra Schwille. Dna nanostructures on membranes as tools for synthetic biology. *Biophysical Journal*, 110(8):1698 – 1707, 2016.
- [39] Vishal Maingi, Jonathan R. Burns, Jaakko J. Uusitalo, Stefan Howorka, Siewert J. Marrink, and Mark S. P. Sansom. Stability and dynamics of membrane-spanning dna nanopores. *Nature Communications*, 8:14784, Mar 2017. Article.
- [40] N. Ponnuswamy, M. Bastings, B. Nathwani, J. Ryu, L. Chou, and M. et al Vinther. Oligolysine-based coating protects dna nanostructures from low-salt denaturation and nuclease degradation. *Nature Communicaitons*, 8:15654, 2017.
- [41] Evi Stahl, Thomas G. Martin, Florian Praetorius, and Hendrik Dietz. Facile and scalable preparation of pure and dense dna origami solutions. *Angewandte Chemie International Edition*, 53(47):12735–12740, 2014.

- [42] Paul WK Rothemund. Folding dna to create nanoscale shapes and patterns. *Nature*, 440(7082):297, 2006.
- [43] Hermann E. Gaub Elias M. Puchner, Bo Huang and Wilhelm Just. Nanopores formed by dna origami: A review. *FEBS Letters*, 588(19):3564–3570, 2014.
- [44] Veikko Linko Coen Gülcher Allard J. Katan Hendrik Dietz Calin Plesa, Adithya N. Ananth and Cees Dekker. Ionic permeability and mechanical properties of dna origami nanoplates on solid-state nanopores. *ACS Nano*, 8(1):35–43, 2014.
- [45] Wilhelm Jahnen-Dechent and Markus Ketteler. Magnesium basics. *Clinical Kidney Journal*, 5(1):3–14, 02 2012.
- [46] Genelink. Maleimide (5') oligo modifications from gene link.
- [47] Dr Nick Oswald. How sds-page works.
- [48] LTD Medical & Biological Laboratories CO. The principle and method of polyacrylamide gel electrophoresis (sds-page).
- [49] Ludwig Reimer. *Transmission electron microscopy: physics of image formation and micro-analysis*, volume 36. Springer, 2013.
- [50] A Bertin and E Nogales. Preparing recombinant yeast septins and their analysis by electron microscopy. In *Methods in cell biology*, volume 136, pages 21–34. Elsevier, 2016.
- [51] Electron Microscopy Sciences. Support film on grids.
- [52] Grid-tech. Plain grids.
- [53] Franz J. Giessibl. Advances in atomic force microscopy. *Rev. Mod. Phys.*, 75:949–983, Jul 2003.
- [54] Martin Langecker, Vera Arnaut, Thomas G. Martin, Jonathan List, Stephan Renner, Michael Mayer, Hendrik Dietz, and Friedrich C. Simmel. Synthetic lipid membrane channels formed by designed dna nanostructures. *Science*, 338(6109):932–936, 2012.
- [55] Stefan Howorka. Building membrane nanopores. *Nature Nanotechnology*, 12:619, Jul 2017. Review Article.
- [56] Avanti Polar Lipids. 4me 16:0 pc.
- [57] S. Pautot, B. J. Frisken, and D. A. Weitz. Production of unilamellar vesicles using an inverted emulsion. *Langmuir*, 19:2870–2879, 2003. Times Cited: 95.

- [58] Laura R. Arriaga, Sujit S. Datta, Shin-Hyun Kim, Esther Amstad, Thomas E. Kodger, Francisco Monroy, and David A. Weitz. Ultrathin shell double emulsion templated giant unilamellar lipid vesicles with controlled microdomain formation. *Small*, 10(5):950–956, 2014.
- [59] Tripta Bhatia, Peter Husen, Jonathan Brewer, Luis A. Bagatolli, Per L. Hansen, John H. Ipsen, and Ole G. Mouritsen. Preparing giant unilamellar vesicles (guvs) of complex lipid mixtures on demand: Mixing small unilamellar vesicles of compositionally heterogeneous mixtures. *Biochimica et Biophysica Acta (BBA) - Biomembranes*, 1848(12):3175 – 3180, 2015.
- [60] Nicoletta Kahya, Dag Scherfeld, Kirsten Bacia, and Petra Schwille. Lipid domain formation and dynamics in giant unilamellar vesicles explored by fluorescence correlation spectroscopy. *Journal of Structural Biology*, 147(1):77 – 89, 2004. Recent Advances in Light Microscopy.
- [61] Ho Cheung Shum, Daeyeon Lee, Insun Yoon, Tom Kodger, and David A. Weitz. Double emulsion templated monodisperse phospholipid vesicles. *Langmuir*, 24(15):7651–7653, 2008. PMID: 18613709.
- [62] Andreas Weinberger, Feng-Ching Tsai, Gijsje H. Koenderink, Thais F. Schmidt, Rosângela Itri, Wolfgang Meier, Tatiana Schmatko, André Schröder, and Carlos Marques. Gel-assisted formation of giant unilamellar vesicles. *Biophysical Journal*, 105(1):154 – 164, 2013.
- [63] Avanti Polar Lipids. What is an suv and luv and how do they differ?
- [64] Jelena Drazenovic, Hairong Wang, Kristina Roth, Jiangyue Zhang, Selver Ahmed, Yanjing Chen, Geoffrey Bothun, and Stephanie L. Wunder. Effect of lamellarity and size on calorimetric phase transitions in single component phosphatidylcholine vesicles. *Biochimica et Biophysica Acta (BBA) - Biomembranes*, 1848(2):532 – 543, 2015.
- [65] Mojca Pavlin, Tadej Kotnik, Damijan Miklavčič, Peter Kramar, and Alenka Maček Lebar. Chapter seven electroporation of planar lipid bilayers and membranes. *Advances in planar lipid bilayers and liposomes*, 6:165–226, 2008.

# 7

## Supplements

### 7.1 FG-Nup Sequences

#### 7.1.1 NSP1

MSKHHHHS GHHHTGHHHHS GSHHHTGENLYFQGSNFNTPQQNKTPFSFGTANNNSNTTN  
QNSSTGAGAFGTGQSTFGFNNSAPNNTNNANSSITPAFGSNNTGNTAFGNSNPTSNVFGSN  
NSTTNTFGSNSAGTSLFGSSSAQQTKSNGTAGGNTFGSSSLFNSTNSNTTKPAFGGLNFG  
GGNNTTPSSTGNANTSNNLFGATANANKPAFSFGATTNDDKKTEPDKPAFSFNSSVGNKT  
DAQAPTTGFSFGSQLGGNKTVNEAAKPSLSFGSGSAGANPAGASQPEPTTNEPAKPALSF  
GTATSDNKTTNTTPSFSFGAKSDENKAGATSKPAFSFGAKPEEKKDDNSSKPAFSFGAKS  
NEDKQDGTAKPAFSFGAKPAEKNNNETSKPAFSFGAKSDEKKDGDASKPAFSFGAKPDE  
NKASATSKPAFSFGAKPEEKKDDNSSKPAFSFGAKSNEDKQDGTAKPAFSFGAKPAEKNN  
NETSKPAFSFGAKSDEKKDGDASKPAFSFGAKSDEKKDS DSSKPAFSFGTKSNEKKDSGSS  
KPAFSFGAKPDEKKNDEVSKPAFSFGAKANEKKEDES KSAFSFGSKPTGKEEGDGAKAA  
ISFGAKPEEQKSSDTSKPAFTFGAQKDNEKKTETSC.

#### 7.1.2 NSP1-S

MSKHHHHS GHHHTGHHHHS GSHHHTGENLYFQGSNSNTPQQNKTPSSSGTANNNSNTTN  
QNSSTGAGASGTGQSTSGSNNSAPNNTNNANSSSTPASGSNNTGNTASGNSNPTSNSSGSN  
NSTTNTSGSNSAGTSSSGSSSAQQTKSNGTAGGNTSGSSSSSNSTNSNTTKPASGGSNSGG  
GNNTTPSSTGNANTSNNSSGATANANKPASSSGATTNDDKKTEPDKPASSNSSSGNKTD  
A QAPTTGSSSGSQSGGNKTSNEAAKPSSSSGSGSAGANPAGASQPEPTTNEPAKPASSSGT  
A TSDNKTTNTTPSSSSGAKSDENKAGATSKPASSSGAKPEEKKDDNSSKPASSGAKSNEDK  
QDGTAKPASSSGAKPAEKNNNETSKPASSSGAKSDEKKDGDASKPASSSGAKPDENKASA  
TSKPASSSGAKPEEKKDDNSSKPASSSGAKSNEDKQDGTAKPASSSGAKPAEKNNNETSKP

ASSSGAKSDEKKDGDASKPASSSGAKSDEKKDSOSSKPASSSGTKSNEKKDSGSSKPASSSG  
AKPDEKKNDESSKPASSSGAKANEEKESDESKSASSSGSKPTGKEEGDGAKAASSSGAKPE  
EQKSSDTSKPASTSGAQKDNEKKTESTSC.

### 7.1.3 Nup57

MGFGFSGSNNGFGNKPAGSTGFSFGQNNNNNTNTQPSASGFGFGGSQPNSGTATTGGFGA  
NQATNTFGSNQQSSTGGGLFGNKPALGSLGSSSTTASGTTATGTGLFGQQTAAQPQQSTIG  
GGLFGNKPTTTTGGLFGNSAQNNSTTSGGLFGNKVGTGSLMGGNSTQNTSNMNAGGLF  
GAKPQNTTATTGGLFGSKPQGSTTNGGLFGSGTQNNNTLGGGGLFGQSQQPQTNTAPGL  
GNTVSTQPSFAWSKPSTGSNLQQQQQQQIQVPLQQTQAIAQQQQLSNYPQQIQEQVLKSK  
ESWDPNTTKTKLRAFVYNKVNETEAILYTKPGHVLQEEWDQAMEKKPSPQTIPIQIYGFE  
GLNQRNQQVTENVAQARIILNHILEKSTQLQKHELDTASRILKAQSRNVEIEKRILKLGTO  
LATLKNRGLPLGIAEEKMWSQFQTLLQRSEDPAGLGKTNELWARLAILKERAKNISSQLDS  
KLMVFNDDTKNQDSMSKGTGEESNDRINKIVEILTNNQQRGITYLNEVLEKDA AIVKKYKN  
KTCHHHHHH

## 7.2 TEM

### 7.2.1 Bare DNA origami

Below are the averaged values of the diameters from the TEM experiments on bare DNA-origami.

Overview of average diameters of bare DNA origami in different buffers

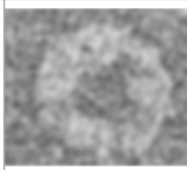
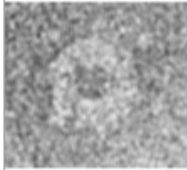
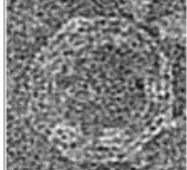
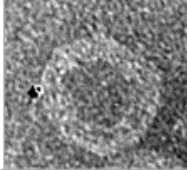
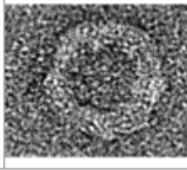
BARE	Inner diameter [nm]	Outer diameter [nm]	Image	Std inner diameter	SD outer diameter
DNA origami buffer	18.033	46.561		$\pm 1.46$	$\pm 1.71$
PBS	25.017	49.295		$\pm 2.84$	$\pm 2.91$
Buffer A	24.482	45.276		$\pm 5.41$	$\pm 7.47$
DNA origami buffer and PBS	21.247	45.852		$\pm 1.57$	$\pm 0.62$
10% Hexandiol and PBS	21.25	45.85		$\pm 1.57$	$\pm 0.62$
Treated with chondroitin (in DNA origami buffer)	23.350	44.235		$\pm 1.81$	$\pm 1.92$

Figure 7.1: Averages of bare DNA origami

### 7.2.2 Coated DNA origami

Below are the averaged values of the diameter from the TEM experiments on coated DNA-origami.

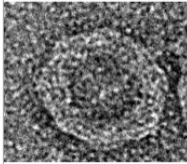
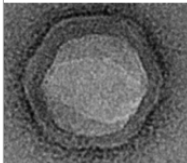
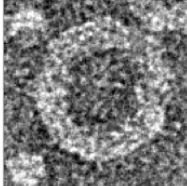
	Inner diameter [nm]	Outer diameter [nm]	Image	Std inner	SD outer
<b>DNA origami buffer</b>	26.420	50.373		$\pm 1.34$	$\pm 1.23$
<b>PBS</b>	29.995	45.075		$\pm 6.61$	$\pm 8.05$
<b>Treated with chondroitin (in DNA origami buffer)</b>	26.233	50.333		$\pm 2.46$	$\pm 1.2$

Figure 7.2: Averages of bare DNA origami

## 7.3 AFM

### 7.3.1 Bare images

The imaged samples of bare DNA-origami are as shown below (Figure 7.3) The corresponding

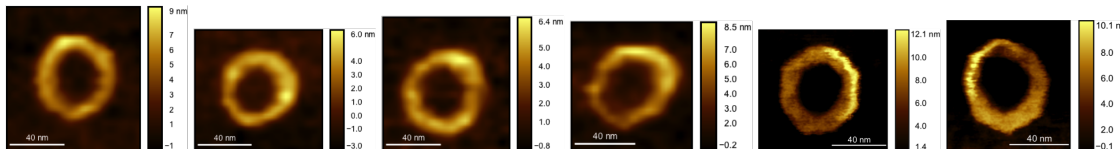


Figure 7.3: All bare DNA-origami images from AFM

volumes of the bare DNA origami are in Figure 7.4)

AFM Bare volumes					
10917.00	15612.00	15048.20	6311	12775	13043

Figure 7.4: Volumes in nm<sup>3</sup>

### 7.3.2 Coated images

The imaged samples of bare DNA-origami are as shown below (Figure 7.6) The corresponding

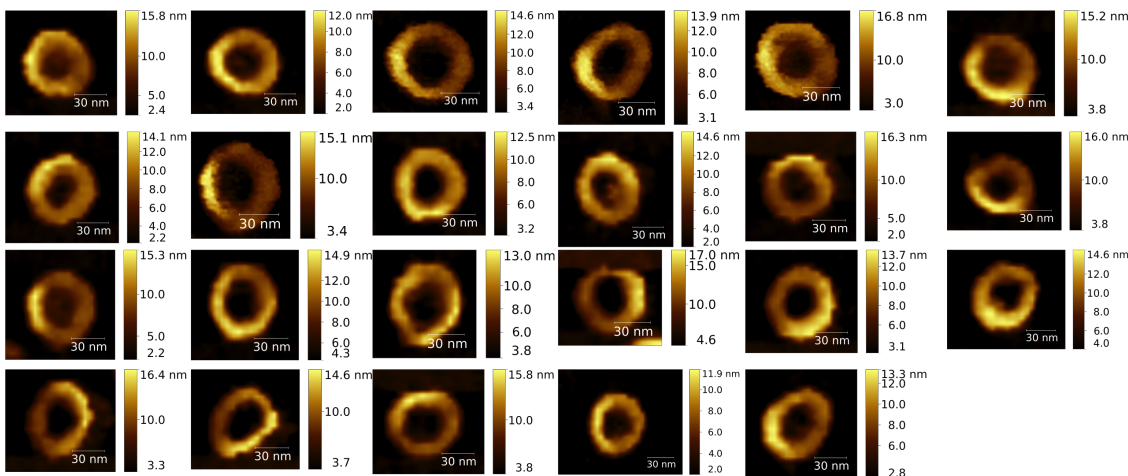


Figure 7.5: All coated DNA-origami images from AFM

volumes of the bare DNA origami are in Figure 7.6)

AFM coated volumes					
25070.00	25982.40	21403.80	18561.00	19545.00	27534.00
28603.00	28977.60	28398.80	24985.00	30305.60	29138.30
27549.70	21466.70	25036.40	24571.60	27894.10	22814.00
26888.00	25601.60	23964.00	25375.70	18684.20	

Figure 7.6: Volumes in nm<sup>3</sup>

### 7.3.3 Comparison Bare Vs Coated

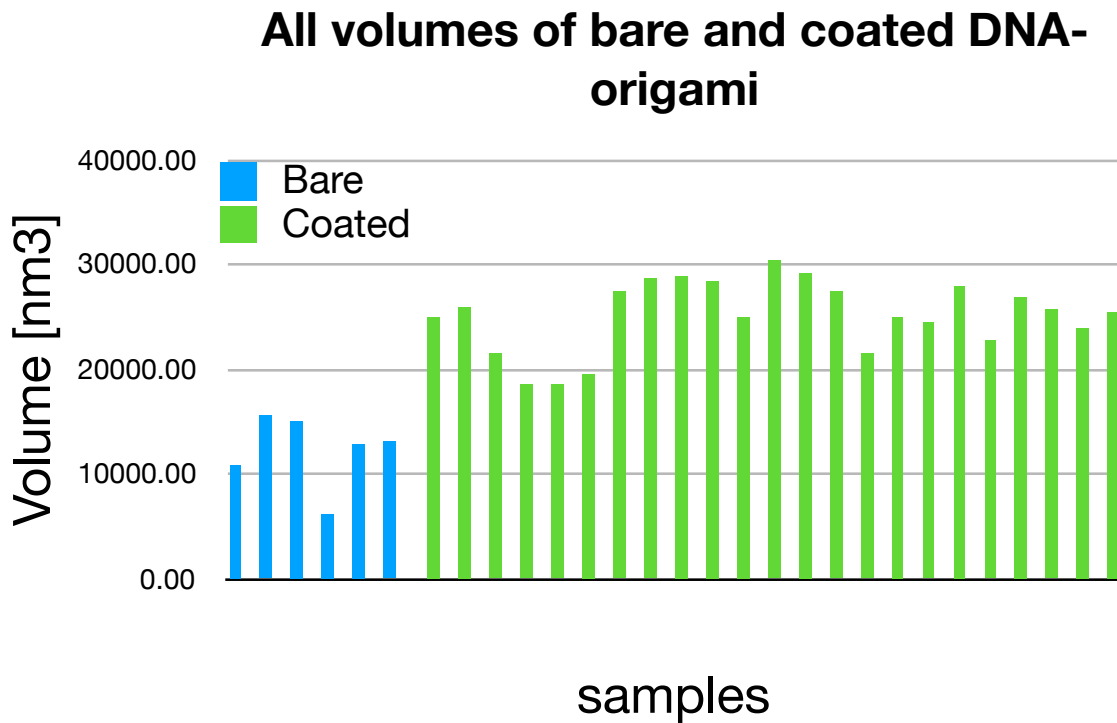


Figure 7.7: volumetric comparison images from AFM

## 7.4 Gels

### 7.4.1 Gel after chondroitin treatment

The below gel shows only the movement of unspecific and unbound NSP1-oligo. Chondroitin was unable to remove the  $K_{10}$ -PEG $_{5K}$  coating from the DNA surface.

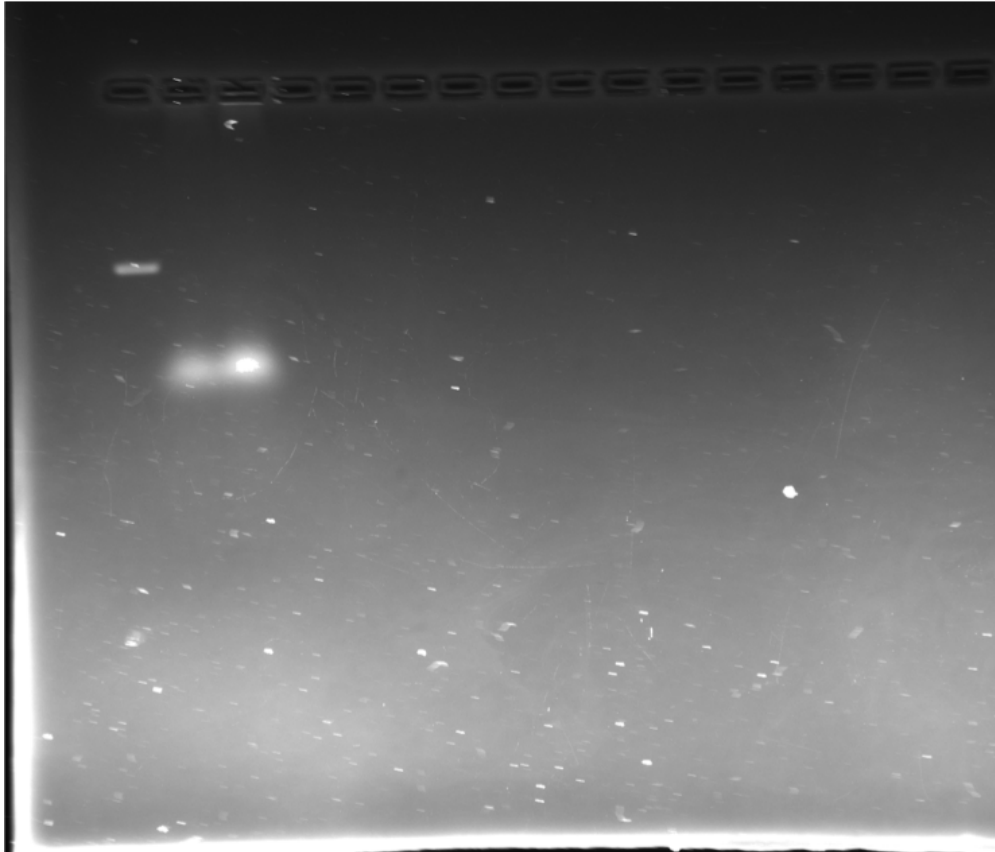


Figure 7.8: Gel cut

### 7.4.2 Gel cutting

In an attempt to extract the NSP1-oligo monomers after ion exchange purification, we ran the NSP1-oligo samples on a gel. In the below image

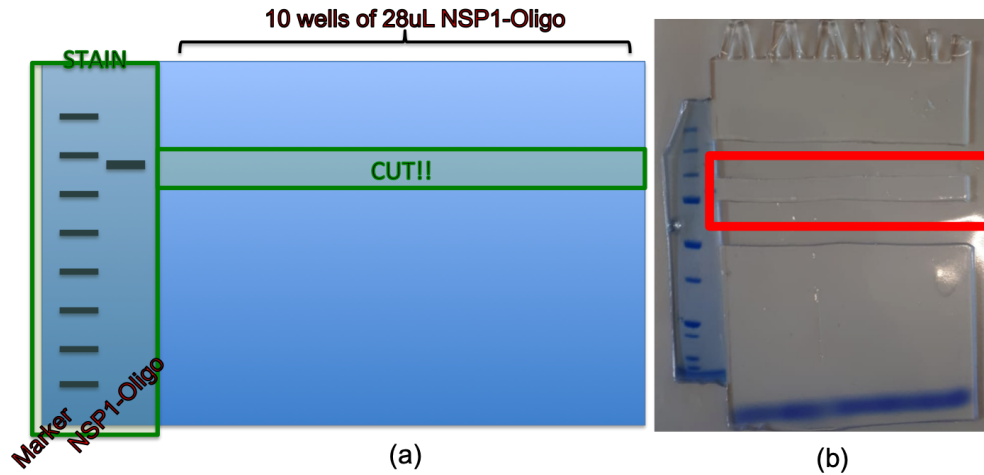


Figure 7.9: Gel cut

## 7.5 protocols

### 7.5.1 TEM stains

#### Uranyl Acetate 2%

1. Weight 0.2 g of uranyl acetate
2. Stir to dissolve the uranyl acetate particles in 10 mL ddH<sub>2</sub>O (can take hours) in the hood.
3. Filter solution with a 0.22  $\mu$ m filter using a syringe
4. Aliquot into eppendoff tubes and wrap with aluminum foil
5. Store at room temperature in the dark
6. Filter again before use after a few days

#### Uranyl formate 2%

- 10 mL ddH<sub>2</sub>O and cool to room temperature
- 10mg uranyl formate in Eppendorf tube to which 0.1 ml of the water is added.
- Vortex vigorously to dissolve yellow powder
- 10 uL in NaOH to the cap of the tube.
- Close the cap and vortex vigorously
- Filter through 0.02  $\mu$ m filter using syringe

### **Uranyl formate 1%**

- 100 mg Uranyl formate into glass bottle with 10 mL ionised water
- Sit overnight under dark condition (Wrap in alufoil)
- Syringe (wrapped in alu-foil) through 0.2 filter
- 1 mL syringe 0.02 um filter
- Aliquot solution into 2ml vials
- Quick freeze.

### **7.5.2 AFM**

#### **Polylysine coating on mica surface:**

1. Cleave mica (3 mm disk)
2. Add 5 ul of 0.01 % polylysine solution (Sigma)
3. Incubate 1 minute
4. Rinse with milliQ water, 1 ml
5. Dry with N<sub>2</sub>

#### **Graphite preparation**

1. HOPG: ZYH quality crystal piece
2. Cleave with scotch tape
3. Blow off loose flakes with N<sub>2</sub> gun

#### **Graphite plasma cleaning**

1. Graphite piece: unknown origin
2. 1 min 100W, 50 mtorr plasmaprep III

#### **Sample deposition**

1. Add 1.8 ul drop to mica disk (more for graphite because of larger size)
2. Incubate in humidity chamber
3. Flush gently using 200 ul of imaging buffer (150/50/5 NaCl/Tris/Mgcl) and two pipettes, keeping sample wet at all times.